C.P. No. 866

C.P. No. 866

MINISTRY OF AVIATION

AERONAUTICAL RESEARCH COUNCIL

CURRENT PAPERS

Tests on an Engine Installation for a Slender Gothic Wing at M = 1·82

by

R. T. Griffiths

LONDON: HER MAJESTY'S STATIONERY OFFICE

1967

PRICE 11*s* 0*d* NET

U.D.C. No. 533.695.17 : 533.6.011.5 : 533.693.3 : 533.691.2

C.P. No. 866
August 1964

TESTS ON AN ENGINE INSTALLATION FOR A SLENDER GOTHIC WING AT M = 1·82

by

R. T. Griffiths

SUMMARY

Tests were made at M = 1·82 over an incidence range of ±10° on an engine installation mounted at the rear of an uncambered slender gothic wing with different values of the boundary layer bleed height and at various mass flow ratios. In addition an investigation was made of the flow conditions at the inboard and outboard edges of the inlet and of the effects of the nacelles on the longitudinal characteristics of the wing. The installation represented a design in which four engines were mounted side by side in each of two nacelles, one on each half of the wing, with the engines partially buried in the wing.

It was found aerodynamically preferable to mount the engines on the lower rather than the upper surface of the wing in order to avoid the possibility of the leading edge vortices entering the intake and to take advantage of the reduced local Mach number present under lifting conditions. With a reasonable boundary layer bleed height, addition of the nacelles to the wing caused a 15% increase in drag, almost independent of incidence. About 30% of this increase was the drag of the boundary layer bleed duct; the remainder could be calculated closely from a knowledge of the nacelle geometry. The nacelles caused small displacements of the lift and pitching moment curves.

Replaces R.A.E. Technical Note No. Aero.2982 - A.R.C. 26912.

CONTENTS

ILLUSTRATIONS

ILLUSTRATIONS (Contd.)

1 INTRODUCTION

A series of tests were planned for the 3 ft × 3 ft wind tunnel at R.A.E. Bedford to investigate various engine installations suitable for slender wings. Choice of nacelle location depends on considerations of structure, wing boundary layer, local Mach number, accessibility, noise and possible interference effects. Several types of installations were examined theoretically in Refs.1 and 2. The installations considered here were for rear mounted engines and since all the models available for test purposes had a central sting fairing, the installations were restricted to separate nacelles at some distance from the wing centre line.

The model for which the intakes were designed was an uncambered gothic wing of aspect ratio 0·75 (Fig.1) which had previously been tested by Squire[3]. An uncambered wing was chosen so that the general characteristics of rear installations for slender wings could be investigated quickly although it was realised that the use of camber might result in different flow conditions at the design incidence for supersonic cruise.

The intakes tested were of the letter-box type with two-dimensional external compression and a boundary layer bleed duct (Figs.2 and 3). Preliminary tests were made to determine the boundary layer profiles at the inboard and outboard edges of the intake: the results of these measurements have already been issued[4].

In addition to the letter-box intakes of the present report, the following other arrangements were included in the series:-

(a) Similar intakes with the outer portions of the wing boundary layer diverted and the central part ducted.

(b) Intakes having vertical compression wedges to incorporate favourable lift interference effects.

2 DESIGN OF THE ENGINE INSTALLATION

The design was based on a full scale aircraft having a centre line chord of 200 ft and geometrically similar to the model chosen (Fig.1) i.e. an integrated aircraft with no separate fuselage. Estimates showed that eight engines of about 4·4 ft gross diameter would be required. It was assumed that the engines would be mounted side by side in two nacelles, one on each wing. Any attempt to design a completely representative engine installation was impracticable at this stage since the main object of the tests was to gather information on the difficulties liable to be encountered and whether the characteristics of the intakes could be predicted closely. The following assumptions about the full scale installation were made in deciding the design of the model to be tested:-

(i) The wing boundary layer would be ducted separately past the engines.

(ii) The intake (Fig.2) would be of single wedge design with a ramp angle of 12° and a lip position angle $\theta_{w\ell} = 46{\cdot}6°$ ($M_{w\ell} = 1{\cdot}8$).

(iii) The main ducts would contract by 3% downstream of the inlet plane followed by a length of constant cross-sectional area to keep the intake shock stable over as wide a range of mass flow as possible.

(iv) The engines would be partially buried in the wing surface. This increased the length of the nacelle to about 25% greater than the aggregate of the lengths of the intake, engine and jet pipe.

(v) Wave drag would be minimised by making the upper surface of the nacelle (except for the cowl lip) parallel with the wing surface and the sides of the nacelle parallel with the free stream direction.

(vi) Although it was realized that the boundary layer thickness would vary across the span, the boundary layer bleed was made of constant height to facilitate testing the model with different values of this bleed height.

There was some controversy as to whether the intakes should be on the upper or lower surface of the wing. A lower surface installation is attractive aerodynamically since the local Mach number is lower than the free stream value and the flow is free from vortices. However a lower surface installation involves possible stone ingestion, bad ditching characteristics and problems of undercarriage location and ground clearance. The present tests were made at both positive and negative incidences to simulate both upper and lower surface installations. The sign convention adopted corresponds to the intakes being on the upper surface.

3 MODEL AND INSTRUMENTATION

In order to fit the nacelles to the wing (Fig.1) with minimum modification to the basic model, the design of the subsonic diffuser and boundary layer bleed duct were adapted in the manner shown in Figs.3,4,5 and 7. The main duct expanded to only 135% of the inlet area (Fig.6) instead of to the corresponding engine frontal area and the bleed duct was led straight along the wing surface instead of passing into the wing in order to bypass the engines. For structural reasons a vertical splitter plate was placed in the centre of each nacelle thus dividing it into two ducts. This plate extended from the front of the subsonic diffuser to the exit. The main duct was complete in itself and was bolted between side plates fixed in slots in the wing surface (Fig.7). Different sets of sideplates were used to vary the boundary layer bleed height. Since the upper surface of the nacelle was to be maintained parallel with the wing surface, the height of the bleed exit was always 0·012 inch higher than the entry, giving bleed duct expansion ratios of 1·05, 1·075 and 1·15 for h = 0·24, 0·16 and 0·08 inch respectively. Exit plugs were provided to test the intake over a range of mass flow (Fig.5).

In order to measure the velocity profiles at the inboard and outboard edges of the intakes at the entry plane two pitot rakes were constructed to fit into the slots in the wing (Figs.8 and 9). Each rake consisted of seven pitot tubes, of inside and outside diameters 0·020 and 0·028 inch respectively. The rakes extended normal to the chordal plane to a distance 0·43 inch from the wing surface. Because of the possibility of interference from the rakes on the

near surface of the wing, the static pressures were measured on the opposite surface at the corresponding negative incidences.

A band of distributed roughness was applied to the leading edge of the wing (Fig.1) to ensure that the boundary layer on the model was turbulent. This consisted of a mixture of carborundum grains and aluminium paint applied so that closely spaced individual grains projected from a paint base about 0·001 inch thick; grade 100 carborundum was used for the tests. The sharp leading edge itself was left clear of roughness.

Measurements of lift, pitching moment and drag were made using a strain gauge balance. The balance measurements were corrected for balance interactions and drift before being reduced to the usual coefficient forms. The pitching moment coefficients are referred to the quarter-chord point of the mean aerodynamic chord. From a consideration of the possible sources of error, together with a study of repeat readings, it is believed that the accuracy of the results from this balance were as follows:-

C_L ±0·003

C_m ±0·0005

C_D ±0·0004 at $C_L = 0$

±0·001 at $C_L = 0·3$.

Pressure recoveries were assessed from pitot rakes at the exit plane(Fig. 10). Each pitot tube consisted of a 0·6 inch length of hypodermic tubing (inside and outside diameters 0·020 and 0·028 inch) fitted to a larger tube of outside diameter 0·047 inch. Details of the tube positions are given in Fig.7. The two outer tubes of the starboard rake were arranged to record base pressure. When exit plugs were inserted, some tubes which had formerly been pitot tubes now recorded plug base pressures. In general no static pressure readings were taken at the exit but for a few check tests, three static tubes were placed in the starboard bleed duct.

4 TESTS

All tests were made at M = 1·82 with a total pressure of 11·6 inches of mercury and total temperature about 25°C, giving a Reynolds number of $2·0 \times 10^6$ (based on aerodynamic mean chord).

Balance readings and exit pressures were recorded over a full range of incidence with various exit plugs and different values of the boundary layer bleed height. Then the intakes were removed and the lift, pitching moment and drag of the wing alone were measured for purposes of comparison. Finally flow visualisation tests were made using the oil flow[5] and vapour screen[6] techniques.

5 DATA REDUCTION AND PRESENTATION OF RESULTS

5.1 Entry plane surveys

The measurements of pitot and static pressures were reduced to velocities, assuming constant static pressure across the boundary layer and no change in total temperature. Logarithmic plots of velocity profiles showed that they conformed to the power law:-

$$\frac{v}{V} = \left(\frac{\eta}{\delta}\right)^{1/n} .$$

Values of the boundary layer thickness δ and the power coefficient n were determined from these logarithmic plots.

5.2 Intake performance

The small exit areas and relatively large size of the pitot tubes limited the number of tubes used. The pitot tubes were arranged to give a horizontal and a vertical pressure distribution across the inboard and outboard ducts with about nine tubes in each duct (Fig.7). It was assumed that the shape of the profile given by the rake would hold for all sections in the duct parallel with the rake. Choking was assumed to take place at the point of maximum total pressure and the static pressure thus given to be constant across the duct exit. Thus mean pressure recoveries at the exit plane were calculated.

5.2.1 Mass flow ratio

The mass flow ratios have been calculated from the continuity equation:-

$$\frac{A_\infty}{A_{en}} = \frac{\bar{P}_{ex}}{P_\infty} \cdot \frac{A_{ex}}{A_{en}} \cdot \left(\frac{A}{A^*}\right)_{M=M_\infty} .$$

5.2.2 Drag coefficient

The drag of the model is presented as external drag where:-

External drag = measured drag - base drag - internal drag.

(i) Measured drag is recorded by the strain gauge balance.

(ii) Base drag correction is applied to give a base pressure equal to the free stream static pressure.

$$D_{base} = (p_\infty - p_{base})\, A_{base} \cos\alpha .$$

(iii) Internal drag is defined as:-

$$D_{int} = m (V_\infty - \bar{V}_{ex} \cos \alpha) + A_{ex} (p_\infty - \bar{p}_{ex} \cos \alpha) \quad .$$

Assuming that the exit is choked and that α is small, substituting the continuity equation we obtain[7]:-

$$C_{D_{int}} = \frac{p_\infty}{q_\infty} \left(1 - \frac{\bar{P}_{ex}}{P_\infty} \cdot B_\infty \right) \frac{A_{ex}}{S} \qquad (1)$$

where

$$B_\infty = 1{\cdot}263 \frac{P_\infty}{p_\infty} - \frac{2q_\infty}{p_\infty} \left(\frac{A}{A^*} \right)_{M=M_\infty} \quad .$$

For assessing the merits of the intake itself it is convenient to consider a drag increment ΔC_D to be added to the basic wing drag to account for the effect of adding the nacelles <u>at constant lift coefficient</u>

$$\Delta C_D = C'_{D_{ext}} - C_{D_{wing}}$$

where

$$C'_{D_{ext}} = C_{D_{meas}} - C_{D_{base}} - C'_{D_{int}}$$

and D'_{int} is the loss in momentum from entry plane to exit (c.f. D_{int} which was from <u>free stream</u> to exit).

Conditions at the entry plane are given by the entry plane surveys. The height of the entering stream tube is determined from the mass flow m and V_{en} is the mean velocity across this stream tube.

It should be noted that the internal drag is for the main duct only and so the bleed drag is included in ΔC_D.

The accuracy of internal drag and base drag is well within the limits already quoted for balance accuracy.

5.3 <u>Boundary layer bleed performance</u>

Pressure recoveries and mass flow ratios are given relative to free stream conditions. Values of mass flow ratio have been calculated using the equation:-

$$\left(\frac{A}{A_{en}}\right)_{Bleed} = \left(\frac{\bar{P}_{ex}}{P_\infty}\right)_{Bleed} \left(\frac{A_{ex}}{A_{en}}\right)_{Bleed} \left(\frac{A}{A^*}\right)_{M=M_\infty} .$$

Owing to the variation of Mach number across the bleed inlet, equation (1) cannot be applied to give the bleed drag. The basic equation has therefore been used:-

$$D = (\bar{V}_{en} - \bar{V}_{ex})\, m \cos\alpha + (p_{en} - p_{ex})\, A_{ex} \cos\alpha + (A_{ex} - A_{en})\,(p_\infty - p_{en} \cos\alpha)$$

$\bar{V}_{en}$ is the mean velocity of the entering stream tube and $\bar{V}_{ex}$ the mean velocity across the exit. p_{en} is known from the entry plane surveys and in the cases for which bleed drag has been considered the value of p_{ex} has been measured by static tubes at the bleed exit.

6 DISCUSSION OF RESULTS

6.1 Entry plane surveys

The entry plane velocity profiles are shown in Fig.11. The outboard boundary layer becomes considerably thinner with increasing incidence such that for $\alpha > 4^\circ$ only one pitot tube remains in the boundary layer and no values of n and δ can be reasonably determined.

Fig.12 shows the variation of n and δ with incidence. It can be seen that the boundary layer profile conforms to a one fifth power law for both inboard and outboard stations practically independent of incidence. This implies relatively large values of the displacement thickness. Similar values of n have been obtained in tests on a slender delta wing at the Aircraft Research Association[8].

The boundary layer thickness inboard is a maximum near zero incidence (δ = 0·28 inch) and decreases slightly with positive or negative incidence. The outboard boundary layer thickness is almost constant at negative incidences (δ = 0·15 inch) but decreases rapidly with positive incidence. It appears that two opposing effects are present. The change in surface Mach number leads to a tendency for the upper surface boundary layer thickness to increase with incidence. Against this, when the incidence is positive the development of the wing leading edge vortices results in a progressive downstream movement of the attachment lines, thereby shortening the run of the boundary layer and reducing the thickness at a given chordwise position downstream of attachment.

Theoretical values of the boundary layer thickness on a flat plate are given for comparison, assuming fully turbulent incompressible flow[9]:-

$$\delta = \frac{0{\cdot}375}{Re_{\xi}^{1/5}}\,\xi \quad \begin{matrix}(0{\cdot}271 \text{ inch (inboard edge)} \\ (0{\cdot}189 \text{ inch (outboard edge)}\end{matrix} .$$

These values are in good agreement with the experimental values (except for the outboard station at high incidence).

Fig.13 shows the variation of Mach number at the entry plane with incidence. The same curve holds for both inboard and outboard stations (within experimental accuracy) and consists of a line of slope 0·012 M/degree for $\alpha > 0$ and of slope 0·018 M/degree for $\alpha < 0$. Also presented in this figure are curves from slender and not-so-slender wing theory (see Appendix). Since these theories apply to attached flow ($\alpha \leqslant 0$ in this case), it appears that the not-so-slender wing theory gives an accurate estimate of the variation of local static pressure with incidence although the estimate of the pressure coefficient at zero incidence is poor.

From the entry plane profiles of total pressure and ρv (similar in shape to the velocity profiles in Fig.11) it is possible to calculate the mean total pressure and mass flow at the entry plane, assuming that the stream tube between η = bleed height, h, and η = h + intake entry height enters the intake. Conditions are known only at the inboard and outboard edges of the intake and conditions between these stations have been calculated assuming that the boundary layer height varies as $\xi^{4/5}$, $\left(\delta = \frac{0{\cdot}375}{\nu}\,\xi^{4/5}\right)$ i.e. practically linearly along the span. This means that any localised change in entry conditions affecting one rake such as the wing vortex moving inboard across the outer rake as incidence is increased, will automatically be assumed to affect the whole intake to a greater extent than would occur in practice.

Fig.14 shows the variation of mean total pressure across the inlet with incidence. For the lower values of bleed height there is an appreciable difference between the total pressures for inboard and outboard ducts, resulting from the thicker boundary layer in front of the inboard duct. At positive incidence the wing vortices form and move progressively inboard from the leading edge, causing a rapid thinning of the boundary layer and an associated rise in pressure recovery. This movement of the wing vortices is clearly illustrated in the vapour screen photographs (Fig.15) and the oil flow photographs (Fig.16). The vapour screen photographs show a view of the starboard side of the model seen from the rear and slightly above the chordal plane with the vapour screen pattern made visible[6] in the intake entry plane. The wing vortex is present at all positive incidence and as the angle of incidence is increased the size of the vortex increases until at $\alpha = 8^{\circ}$ it reaches the outboard side of the nacelle. For $\alpha > 8^{\circ}$ the vortex enters the intake causing a decrease in pressure recovery of the outboard duct owing to reduced total pressure in the vortex core.

Curves showing the variation of full mass flow at the entry plane with incidence are given in Fig.17. Mass flow decreases almost linearly with incidence except for $\alpha > 4^{\circ}$ where the boundary layer is affected by the wing

vortices. With a reasonably large value of the boundary layer bleed height the mass flow ratio exceeds unity at high negative incidences since the local Mach number is less than the free stream Mach number.

6.2 Intake performance

6.2.1 Pressure recoveries

Since the boundary layer thickness varies with incidence and spanwise position and since the mass flow varies with incidence, parameters h (boundary layer bleed height) and $\frac{A_{ex}}{A_{en}}$ (ratio of exit area to entry area) have been chosen in preference to $\frac{h}{\delta}$ and $\frac{A_{\infty}}{A_{en}}$.

Fig.18 shows a typical set of pressure distributions across the exit for $\frac{A_{ex}}{A_{en}} = 0{\cdot}86$. These illustrate the effect of bleed height on the distribution in each duct. A spanwise gradient is present for the lower values of bleed height giving rise to a higher pressure recovery outboard. This disappears for h = 0·24 inch and at higher incidences there is a tendency to form an opposite gradient.

These pressure distributions are typical of those obtained for each value of $\frac{A_{cx}}{A_{en}}$ $\left(\frac{A_{ex}}{A_{en}} = 1{\cdot}02 \text{ is more rounded}\right)$, whereas the vertical distribution (Fig.19) varies considerably.

Fig.19a shows that for $\frac{A_{ex}}{A_{en}} = 1{\cdot}02$ the pressure distribution is extremely poor and indicates that the intake flow is supercritical. As incidence (and therefore entry plane Mach number) is increased the pressure distribution becomes worse (Fig.19b). Variation of h affects mass flow and mean entry plane Mach number (Fig.19c).

A complete set of curves showing the variation of mean pressure recovery with incidence is given in Fig.20. The characteristics of Fig.14 are present i.e. the difference in pressure recovery between inboard and outboard ducts can be seen, as can also a rapid increase of pressure recovery in the outboard duct with incidence for $\alpha > 4^{\circ}$ (for the lower values of h) until the wing vortex enters the intake. These results show that under-wing intake will give better pressure recoveries than intakes on the upper surface, provided the wing boundary layer is in either case removed.

The schlieren photographs in Fig.21 illustrate shock patterns at $\alpha = -10^{\circ}$, 0 and 10°.

Curves of pressure recovery against mass flow are presented in Fig.22 for $\alpha = -4^{\circ}$, 0 and 4° (4° is approximately the cruising incidence) together with estimated values of the peak recovery.

In general the pressure recovery is higher in the outboard duct with peak values of 0·82, 0·80 and 0·77 for $\alpha = -4°$, 0 and 4° respectively. For the lower values of h the reduced Mach number in the boundary layer results in the shock-wave from the wedge compression surface lying ahead of the cowl lip thus giving a maximum mass flow lower than that indicated in Fig.17. An unexpected feature of these results is that for the outboard duct the pressure recoveries are higher for h = 0·16 inch than for h = 0·24 inch. This may be due to some softening of the wedge shock when some boundary layer air is flowing into the intake, i.e. a near isentropic compression fan replaces the single shock-wave over part of the entry plane and gives rise to more efficient compression.

The measured values of pressure recovery fall short of the estimates given in Fig.22. These theoretical values are estimated from a consideration of losses made up as follows:-

(1) External losses

This includes the pressure loss through the wing bow wave and the friction losses over the wing surface. The skin friction losses are zero when $h > \delta$ and for h = 0·24 inch the external losses are less than 1% except for $\alpha > 8°$ when the outboard edge of the duct lies in the region of low total pressure in the wing vortex.

(2) Shock losses

Shock losses vary with entry plane Mach number and therefore with incidence. The maximum pressure recovery obtainable decreases with Mach number and when the wedge shock wave falls inside the cowl lip (i.e. when $M_{en} > 1·8$) the pressure recovery falls even more rapidly since part of the entering stream tube passes through only a normal shock.

(3) Interference losses

Seddon and Haverty[10] have shown the existence of interference losses due to the interaction between the normal shock and the boundary layer on the ramp. Their empirical formula for these losses show that for this intake, owing to the length of constant cross-sectional area at the throat, the interference losses with $h > \delta$ are negligibly small.

(4) Internal skin friction losses

Since the pressure recoveries have been measured at the exit plane, rather than at the engine compressor face position, and since the Reynolds number and hydraulic radius of the ducts are small, the friction losses are high - about 5 or 6% in pressure recovery. The losses are calculated from the formula:-

$$\frac{\Delta P}{q_2} = C_f \int_{\text{entry}}^{\text{exit}} \left(\frac{A_i}{A}\right)^2 \frac{B}{A}\, dx$$

where q_2 = dynamic pressure behind normal shock-wave

C_f = skin friction drag coefficient

A = duct cross sectional area

B = perimeter at any station x.

6.2.2 Drag

Curves showing the external drag of the complete model at $\alpha = 0$ are given in Fig.23. A clearer picture of the drag penalty incurred by the nacelles is gained from Fig.24 which shows the variation of ΔC_D with mass flow for different values of boundary layer bleed height. Minimum drag is at full mass flow and varies from $\Delta C_D = 0{\cdot}0013$ for h = 0 to $\Delta C_D = 0{\cdot}0021$ for h = 0·24 inch. At reduced mass flow the drag rises owing to flow spillage. Included in Fig.24 are theoretical estimates for the cowl drag and external skin friction drag and the measured bleed drag. These are the three components of ΔC_D and it can be seen that the estimates are in good agreement with the practical results. The estimate for cowl drag includes the drag due to the chamfer on the leading edges of the side plates and was calculated using Ackeret's theory. Skin friction drag was calculated for the side and top surfaces of the nacelle, allowance being made for the wing surface which was covered by the nacelle. No allowance was made for corner interference effects which would be small. The bleed drag has actually been measured in the tests but it should be noted that for a practical installation the bleed duct will have a more tortuous path in bypassing the engine and a consequent increase in drag. A check on the value of bleed drag is given by comparing the values of ΔC_D for h = 0 and h = 0·24 inch. The difference is almost entirely due to bleed drag and it does in fact correspond with the directly measured value of bleed drag for h = 0·24 inch i.e. $C_{D_{bleed}} = 0{\cdot}0007$ (Fig.26).

Taking h = 0·16 inch as a practical value for the boundary layer bleed height the drag increment ΔC_D (as a percentage of the basic wing drag C_{D_o}) is made up as follows:-

Bleed drag	4·1
External skin friction	3·1
Cowl drag	7·3
	14·5% C_{D_o}

The variation of ΔC_D (h = 0·16 inch, full mass flow) with lift coefficient is shown in Fig.25. The values were derived from the faired curves of axial force against lift coefficient. ΔC_D is practically constant with C_L although there is a slight increase as C_L increases, owing to the pressure interference between nacelle and wing causing a change in lift coefficient at a given angle of incidence. This effect is favourable to the underwing installation (the negative incidence results as shown).

6.3 Boundary layer bleed performance

Fig.26 shows the variation of bleed duct pressure recovery, mass flow and drag with boundary layer bleed height h. Values of δ are given in the upper right hand corner of the figure so that h/δ may be calculated if required.

Pressure recovery and mass flow ratio increase with h to give encouragingly high results which suggest that the bleed duct is working efficiently in spite of its simple design. Indeed, for h = 0·24 inch the mass flow is higher than the theoretical estimate for a 1/5 power law boundary layer given in Ref.12. This theoretical curve has been calculated using the mean value of the boundary layer thickness and the mass flows have been related to free stream conditions.

The variation of pressure recovery with incidence is similar to the behaviour of the main intake duct at h = 0. There is a decrease in pressure recovery with increase of incidence until, above $\alpha = 4^\circ$, a thinning of the boundary layer by the effect of wing vortex flow causes a rapid increase. This increase continues until at $\alpha = 10^\circ$ the pressure recovery has almost returned to its value at $\alpha = -10^\circ$.

Bleed drag appears to vary linearly with h, the coefficient value being 0·00070 at h = 0·24 inch for $\alpha = 0$. As mentioned earlier this tallies with estimates of bleed drag from a consideration of overall intake drag for varying values of h.

6.4 Lift and pitching moment

A typical lift curve is shown in Fig.27 compared with the curve for the basic wing. The intakes (on the top surface) cause a decrease in lift which is independent of incidence in the range considered. This change in lift does not appear to depend in a consistent way on mass flow or boundary layer bleed height, although this is difficult to assess since the values of ΔC_L approach the limits of experimental accuracy. The mean value of ΔC_L obtained from all the tests ($\Delta C_L = -0·0065$) is within 10% of an estimated value taking into account the lift on the cowl and ramp surfaces and the change in pressure distribution on the wing caused by external chamfer on the sides of the nacelles.

The pitching moment curves (Fig.28 shows a typical example) are also unaffected in slope by the addition of the intakes and again there is no

consistent trend with mass flow or boundary layer bleed height. The mean shift is $\Delta C_m = +0{\cdot}0032$ at constant incidence and the corresponding value from the lift forces already calculated is the same (ΔC_m due to the drag increment is small). Making allowance for the change of zero-lift angle ($0{\cdot}29°$) this leads to a mean result at constant lift:-

$$\Delta C_m = 0{\cdot}0019 \quad .$$

7 CONCLUSIONS

Tests at $M = 1{\cdot}82$ on a rear wing installation for four engines side-by-side in each of two nacelles, one on each half of an uncambered slender gothic wing, led to the following conclusions:

(1) From an aerodynamic point of view an under surface installation is preferable to an upper surface one owing to the decreased local Mach number and the absence of wing vortices.

(2) With a suitable boundary layer bleed height, the drag of the intakes at zero lift amounted to approximately 15% of the wing drag. This value agreed closely with the sum of a skin friction increment (20%), estimated from the increase in wetted area, a cowl drag (50%), estimated for the basic nacelle shape in isolation and the internal drag of the bleed (30%), measured in the experiment.

(3) The variation of intake drag (at constant C_L) with C_L was small; favourable to an underwing rather than an overwing installation.

(4) The intakes had only small effects on lift and pitching moment: these could be predicted from a knowledge of nacelle geometry.

(5) The profile of the undisturbed wing boundary layer at the position of the entry plane conformed approximately to a one-fifth power law.

(6) The boundary layer thickness on the wing upper surface at the position of the outboard edge of the intake was observed to decrease rapidly as the wing vortex moved inboard with increase of incidence (above about 4° in this case).

SYMBOLS

x, y, z	co-ordinate system
s	semi span at trailing edge
c_o	root chord
S	wing area
q	free stream dynamic pressure
M	Mach number
α	angle of incidence
v	local velocity
V	velocity just outside the boundary layer
η	distance from surface, normal to chordal plane
δ	boundary layer thickness
n	"power coefficient" where $\frac{v}{V} = \left(\frac{\eta}{\delta}\right)^{1/n}$
h	boundary layer bleed height
ξ	chordwise distance from leading edge
Re	local Reynolds number based on ξ
ν	kinematic viscosity
p	static pressure
P	total pressure
A	area
m	mass flow
C_L	lift coefficient = $\frac{L}{qS}$
C_m	pitching moment coefficient = $\frac{m}{qS\bar{c}}$ (referred to quarter-chord point)

SYMBOLS (Contd.)

C_D drag coefficient $= \frac{D}{qS}$

$\Delta(\ )$ change in ( ) due to adding the intakes to the wing at constant lift coefficient

Suffices

$(\ )^*$ when the local speed equals the speed of sound

$(\ )_{en}$ at the entry plane

$(\ )_{ex}$ at the exit plane

$(\ )_{\infty}$ in the free stream

$(\ )_{int}$ internal

$(\ )_{ext}$ external

$\overline{(\ )}$ mean value across the exit.

REFERENCES

No.	Author	Title, etc.
1	De Havilland Aircraft Company Ltd.	Engine installation for slender delta aircraft. D.H. Aero Dept/A.74/MJH August, 1957.
2	De Havilland Aircraft Company Ltd.	Comparison of engine installations for slender delta aircraft. ARC 20728 October, 1957.
3	Squire, L.C.	An experimental investigation at supersonic speeds of the characteristics of two gothic wings, one plane and one cambered. ARC R&M 3211. May, 1959.
4	Griffiths, R.T.	Some boundary layer measurements on a slender gothic wing at supersonic speeds. ARC 22,058 Feb.1960.
5	Stanbrook, A.	The surface oil flow technique as used in high speed wind tunnels in the United Kingdom. ARC 22,385 August, 1960.

REFERENCES (Contd.)

No.	Author	Title, etc.
6	McGregor, I.	Development of the vapour screen method of flow visualisation in the 3ft tunnel at R.A.E. Bedford. R.A.E. Tech Note Aero 2709. August, 1960.
7	Frankel, L.E.	The external drag of some pitot-type intakes at supersonic speeds, Pt.1. ARC 13537 June, 1950.
8	Sharp, A.W.	Some data on the flow field in depth around a slender delta wing at supersonic speed. ARC 21967 May, 1960.
9	Piercy, N.A.V.	Aerodynamics. The English Universities Press Ltd.
10	Seddon, J. Haverty, L.	Results from unpublished R.A.E. Test.
11	Igglesden, M.S.	Wind tunnel measurements of the lift-dependent drag of thin conically cambered slender delta wings at Mach numbers 1.4 and 1.8. ARC CP 519 April, 1960.
12	Simon, P.C. Kowalski, K.L.	Charts of boundary-layer mass flow and momentum for inlet performance analysis Mach number 0.2 to 5.0. N.A.C.A. Tech Note 3583. November 1955.
13	Jones, R.T.	Properties of low-aspect-ratio pointed wings at speeds below and above the speed of sound. N.A.C.A. Report 835, 1946.
14	Adams, M.C. Sears, W.R.	Slender-body-theory - Reviews and extension. Journal of the Aeronautical Sciences. Volume 20 page 85. Feb. 1953.
15	Squire, L.C.	Some applications of 'not-so-slender wing' theory to wings with curved leading edges. ARC R&M 3278.

APPENDIX

ESTIMATION OF THE VARIATION OF ENTRY PLANE MACH NUMBER WITH INCIDENCE

Squire[3] has quoted pressure coefficients of -0·093 and -0·088 for stations on the wing corresponding to the inboard and outboard edges of the intake at the entry plane at $\alpha = 0$. These give:-

$$\left.\begin{array}{lll} \text{Inboard} & M_{en} & = 1{\cdot}972 \\ \text{Outboard} & M_{en} & = 1{\cdot}962 \end{array}\right\} \quad \alpha = 0 \ .$$

Slender body theory

Jones[13] slender body theory shows that:-

$$\frac{\Delta p_L}{q} = \frac{4\,\alpha\, s'(X)}{\sqrt{1-\psi^2}}$$

where Δp_L is the difference in static pressure between upper and lower surface

α is in radians

X is $\frac{x}{c_o}$

$s(X)$ is the equation of the leading edge; in this case $s(X) = \frac{X}{4}(2 - X)$

$s'(X)$ is $\frac{d}{dX}[s(X)]$

ψ is $y \div$ local semispan.

Applied to this model and Mach number we have:-

$$\text{Inboard} \quad \frac{\Delta p_L}{P_\infty} = 0{\cdot}001824\,\alpha$$

$$\text{Outboard} \quad \frac{\Delta p_L}{P_\infty} = 0{\cdot}002222\,\alpha$$

with α now in degrees.

These give the curves in Fig.13 (which are not straight lines since M does not vary linearly with p/P).

Not-so-slender wing theory

Adams and Sears theory[14] has been developed by Squire[15] to give:-

$$\frac{\Delta p_L}{q} = 4\alpha\left[1 + F(X)\,\beta^2 s_T^2 + G(X)\,\beta^2 s_T^2 \log_e \beta s_T\right] \frac{s'(X)}{\sqrt{1-\psi^2}}$$

$$+ 4\alpha\left[F'(X)\,\beta^2 s_T^2 + G'(X)\,\beta^2 s_T^2 \log_e \beta s_T\right] s(X)\sqrt{1-\psi^2}$$

where F(X) and G(X) are functions of the Jones slender body theory load distribution.

s_T is ratio of trailing edge semi span to root chord and $\beta = \sqrt{M^2 - 1}$.

For this model and Mach number we have:-

$$\text{Inboard } \frac{\Delta p_L}{P_\infty} = 0{\cdot}003798\,\alpha$$

$$\text{Outboard } \frac{\Delta p_L}{P_\infty} = 0{\cdot}003869\,\alpha$$

which give the relations of M_{en} with α presented in Fig.13 and predicts exactly the static pressure differences between upper and lower surface measured at the entry plane (for attached flow).

TABLE

Details of model

Wing

Root chord	20 inches
Span	10 inches
Area	133·3 sq inches
Volume	72 cubic inches
Aspect ratio	0·75
Aerodynamic mean chord	15 inches
Thickness chord ratio	8·2%
Body diameter	1·35 inches
Cross section	Diamond
Planform given by	$\frac{y}{s} = \frac{x}{c_o}\left(2 - \frac{x}{c_o}\right)$
Centre line section given by	$\frac{z}{c_o} = 0{\cdot}126\,\frac{x}{c_o}\left(1 - \frac{x}{c_o}\right)\left\{2 - 2\,\frac{x}{c_o} + \left(\frac{x}{c_o}\right)^2\right\}$

Intakes

Inboard edge	y = 0·92 inch
Outboard edge	y = 2·88 inches
Leading edge	x = 14·8 inches
Trailing edge	x = 20·0 inches
Height of upper surface above wing surface with h = 0·24 in.	0·53 inch
Ramp angle	12°
Inside lip angle	8°
Shock on lip Mach number	M_{wc} = 1·80
Internal contraction	3·1%
Main duct capture area (both nacelles)	0·72 square inch
Boundary layer bleed duct height	0, 0·08, 0·16 and 0·24 inch

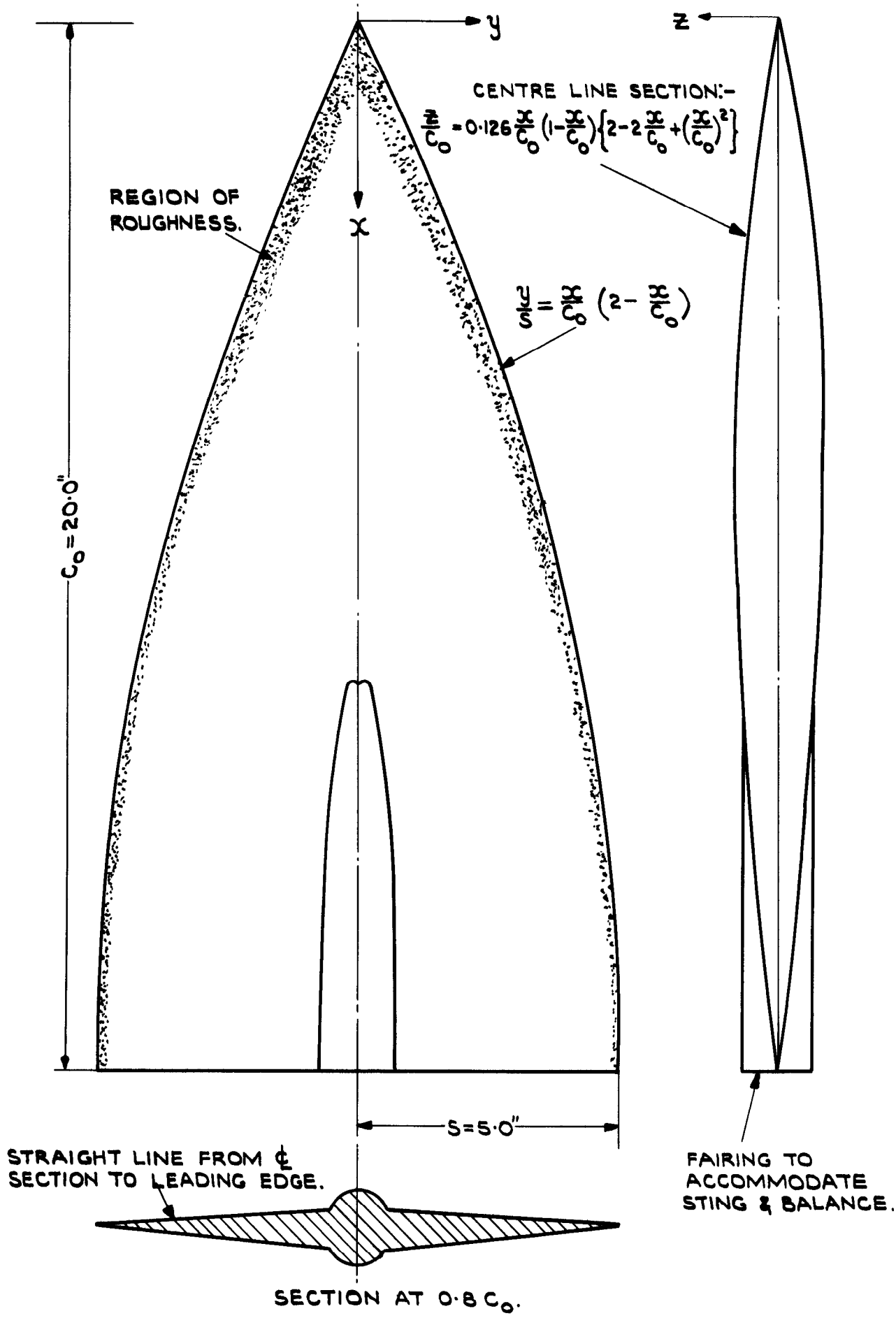

FIG. 1. DETAILS OF WING.

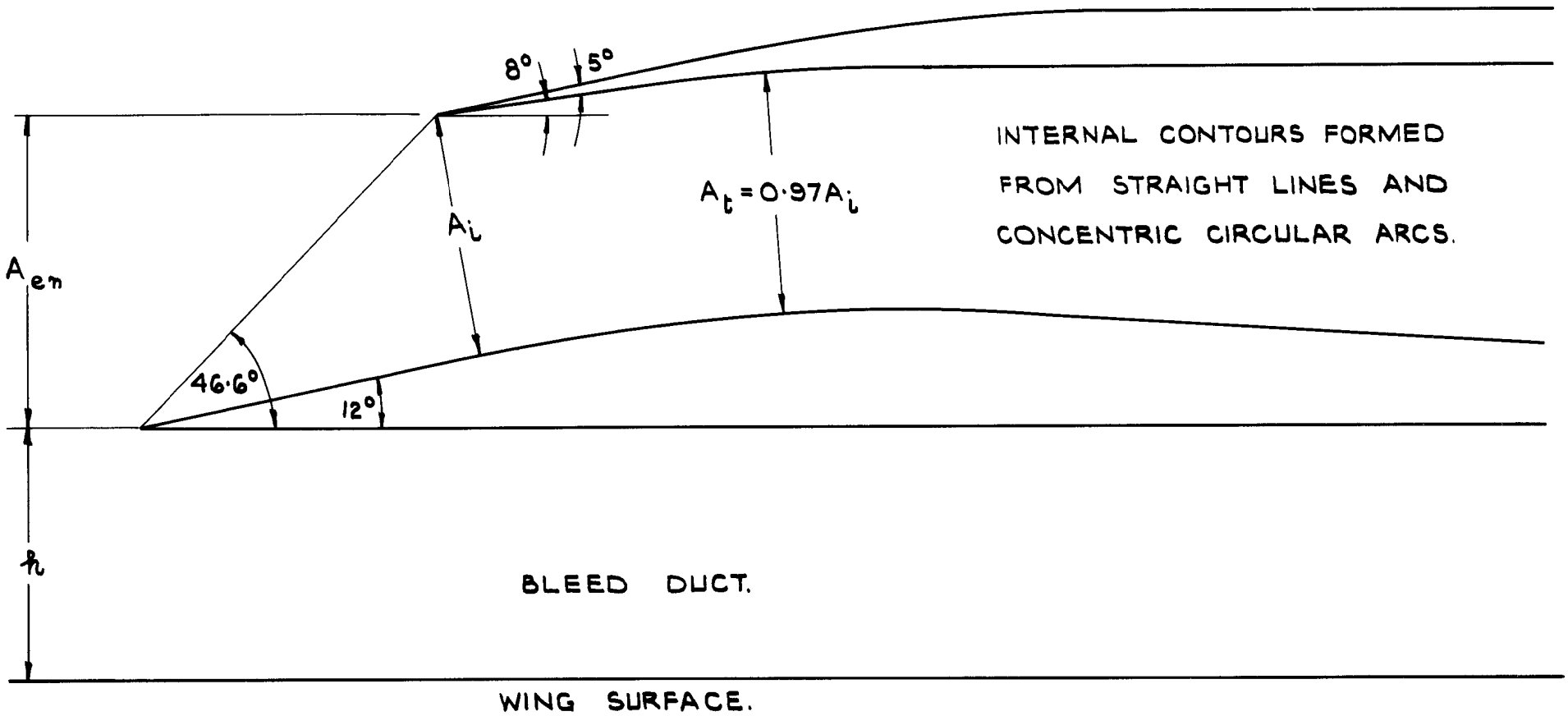

FIG. 2. INTAKE GEOMETRY.

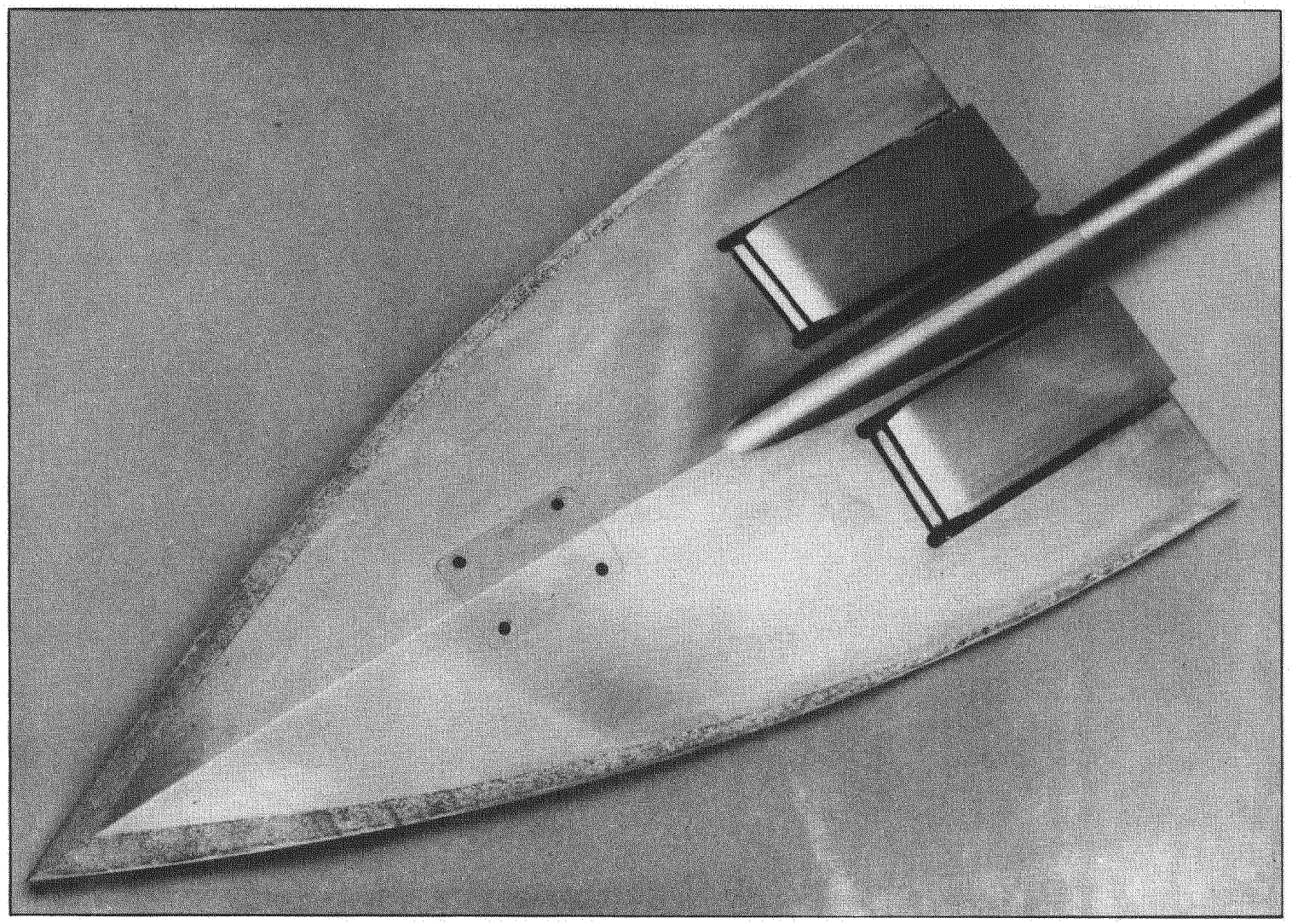

FIG.3. MODEL WITH INTAKES

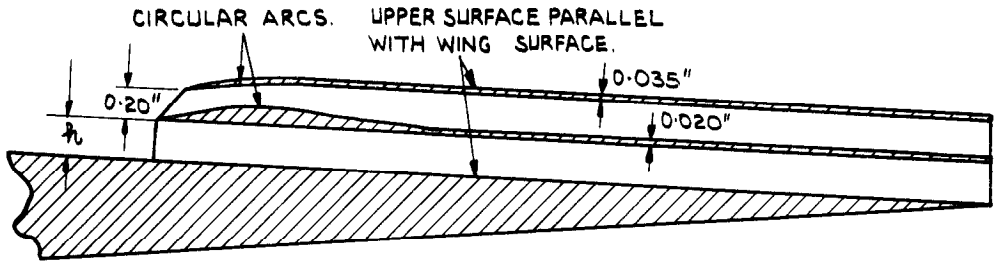

FIG. 4. SECTION THROUGH INTAKE.

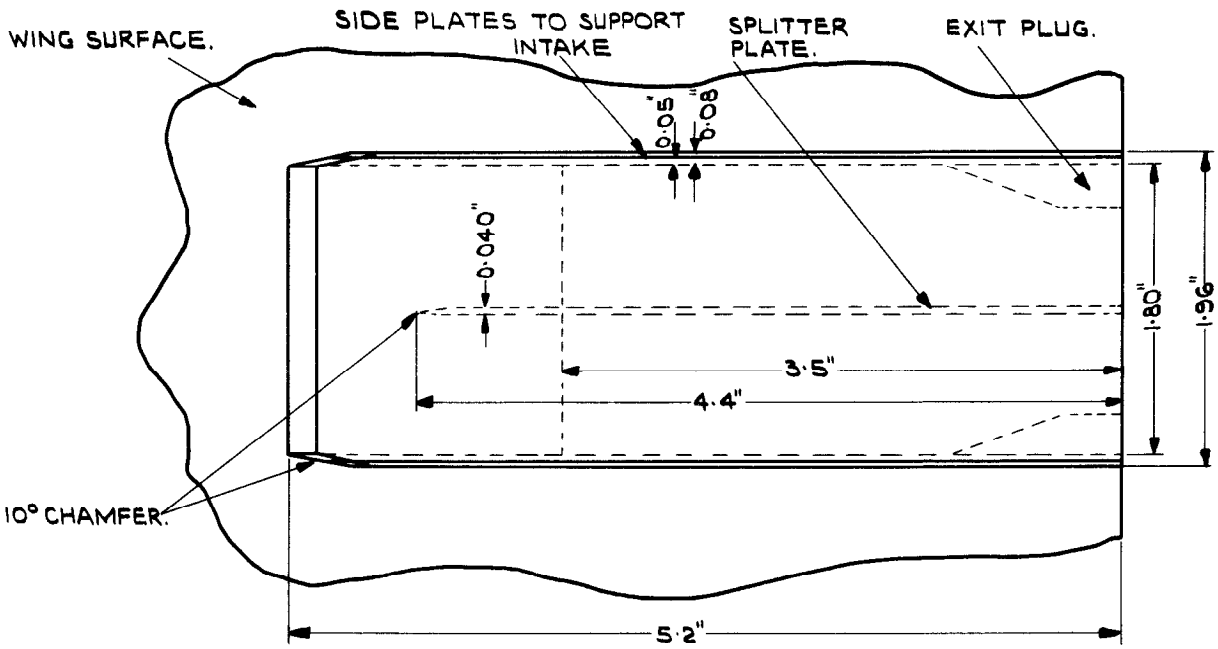

FIG. 5. PLAN VIEW OF INTAKE.

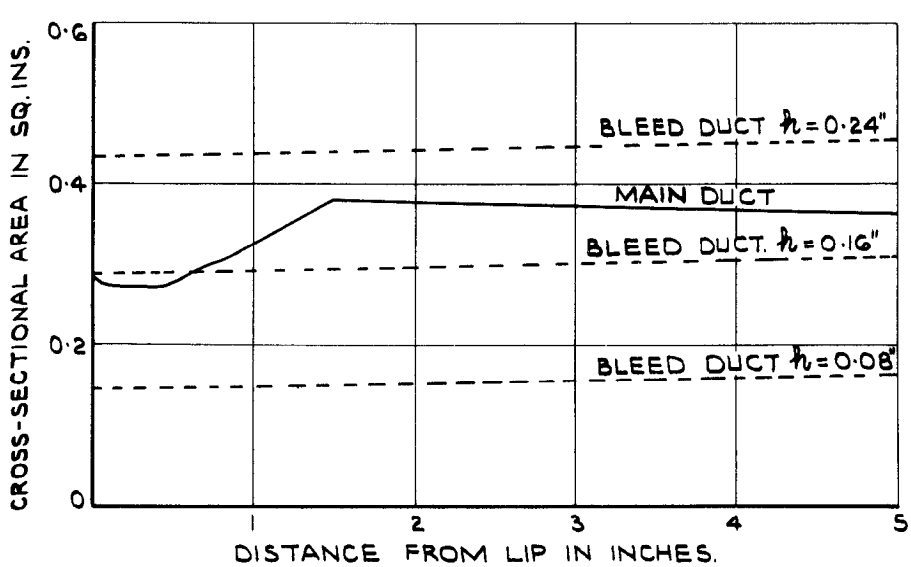

FIG. 6. AREA DISTRIBUTION.

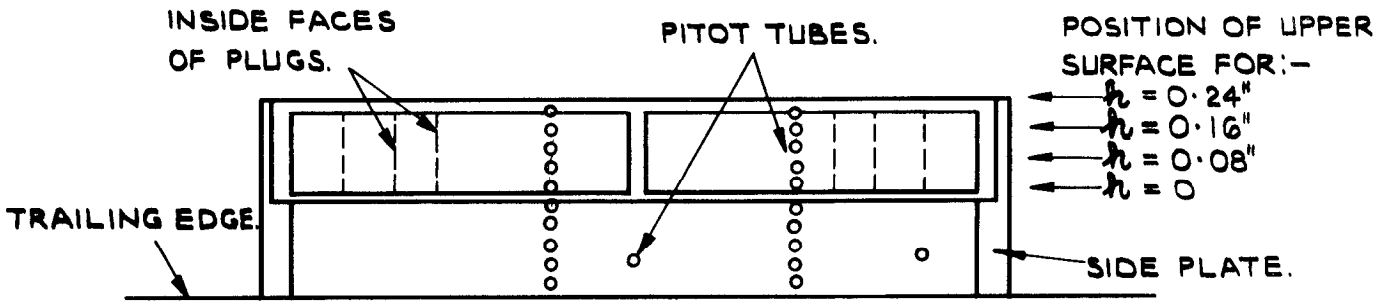

THE PORT NACELLE PITOT RAKE IS FIXED IN SPACE WHILE THE MAIN DUCT "BOX" IS PLACED BETWEEN DIFFERENT SIDE PLATES TO GIVE VARIOUS VALUES OF h AS SHOWN.

(a) PORT NACELLE.

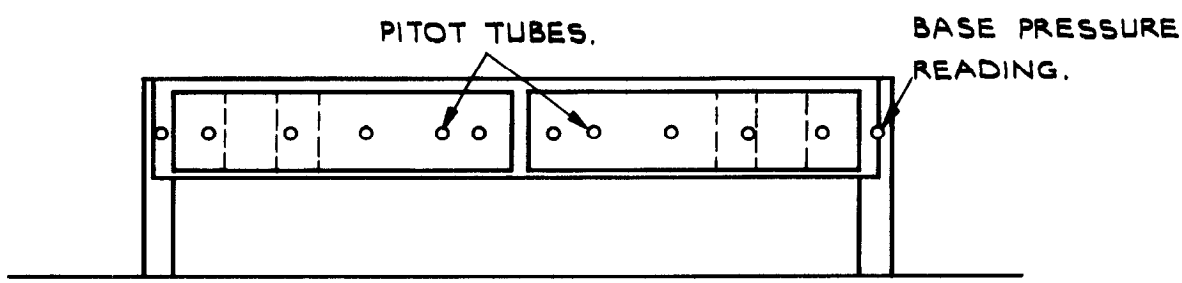

FOR DIFFERENT BLEED HEIGHTS h THE STARBOARD PITOT RAKE MOVES WITH THE MAIN DUCT "BOX" SO TO MAINTAIN THE SAME RELATIVE POSITION.

(b) STARBOARD NACELLE.

(N.B. BOTH VIEWS ARE UPSTREAM.)

FIG. 7. REAR VIEWS OF NACELLES SHOWING PITOT RAKE POSITIONS.

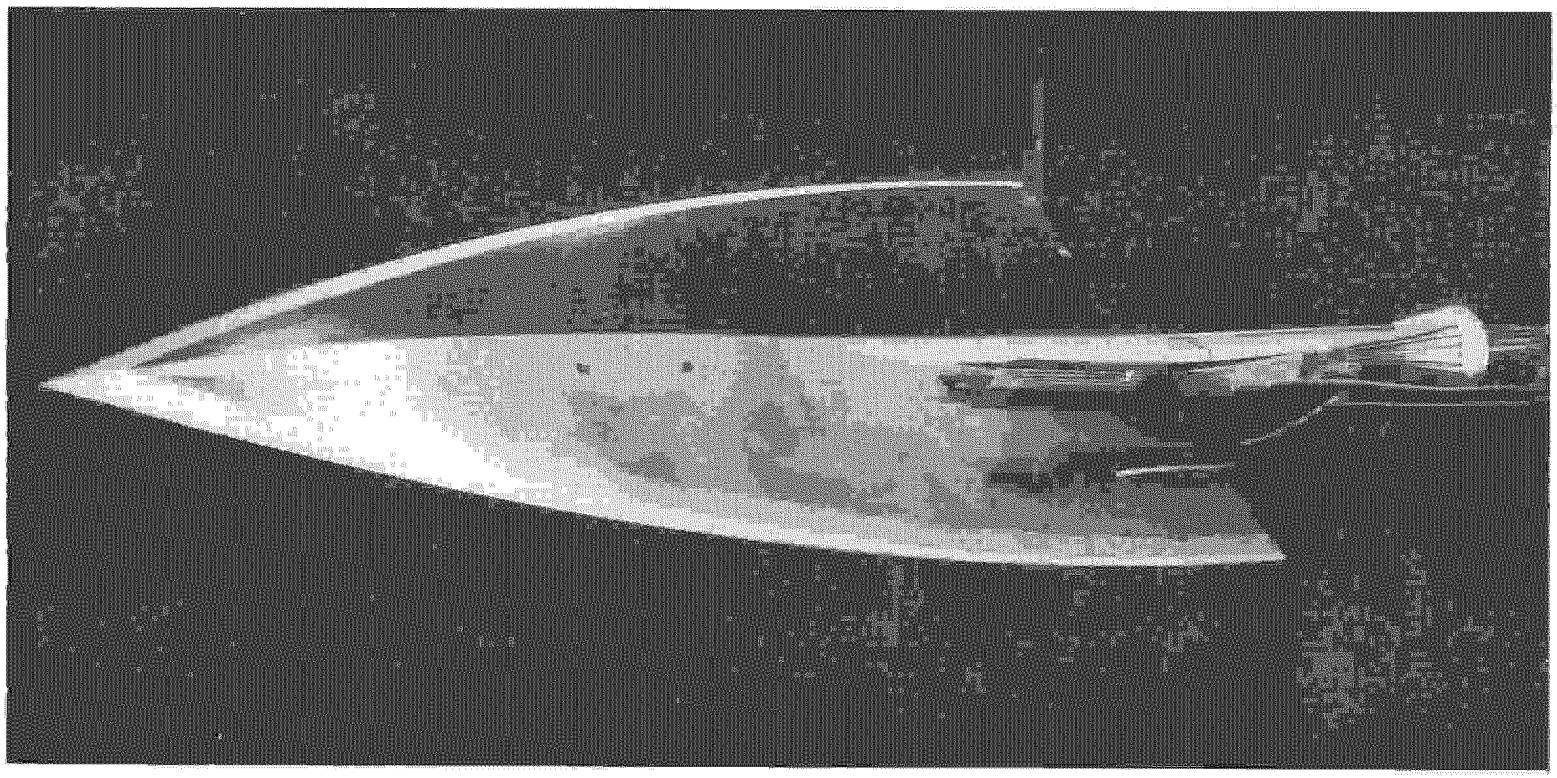

FIG.8. MODEL WITH ENTRY PLANE PITOT RAKES

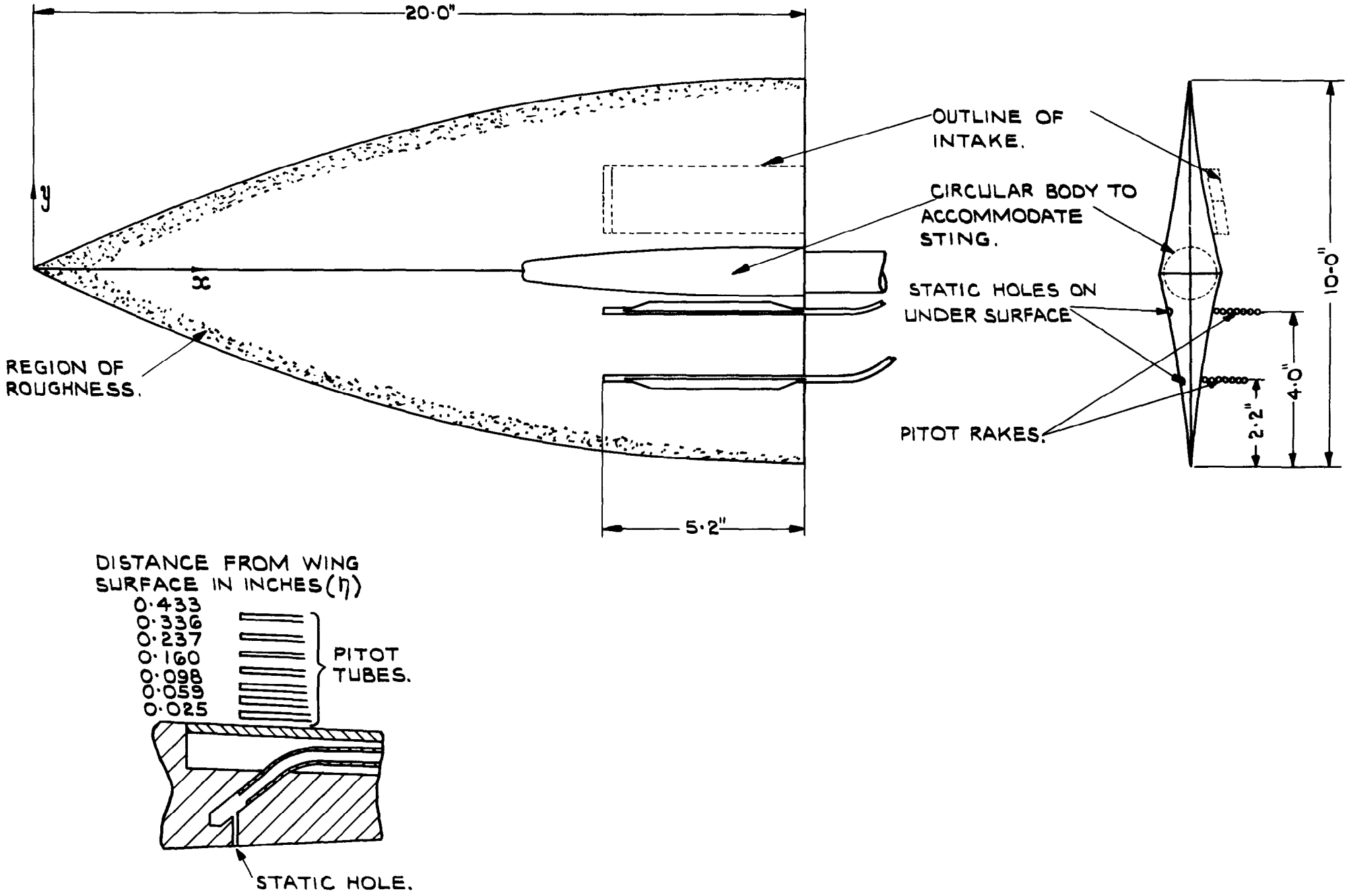

FIG. 9. DETAILS OF MODEL WITH ENTRY PLANE PITOT RAKES.

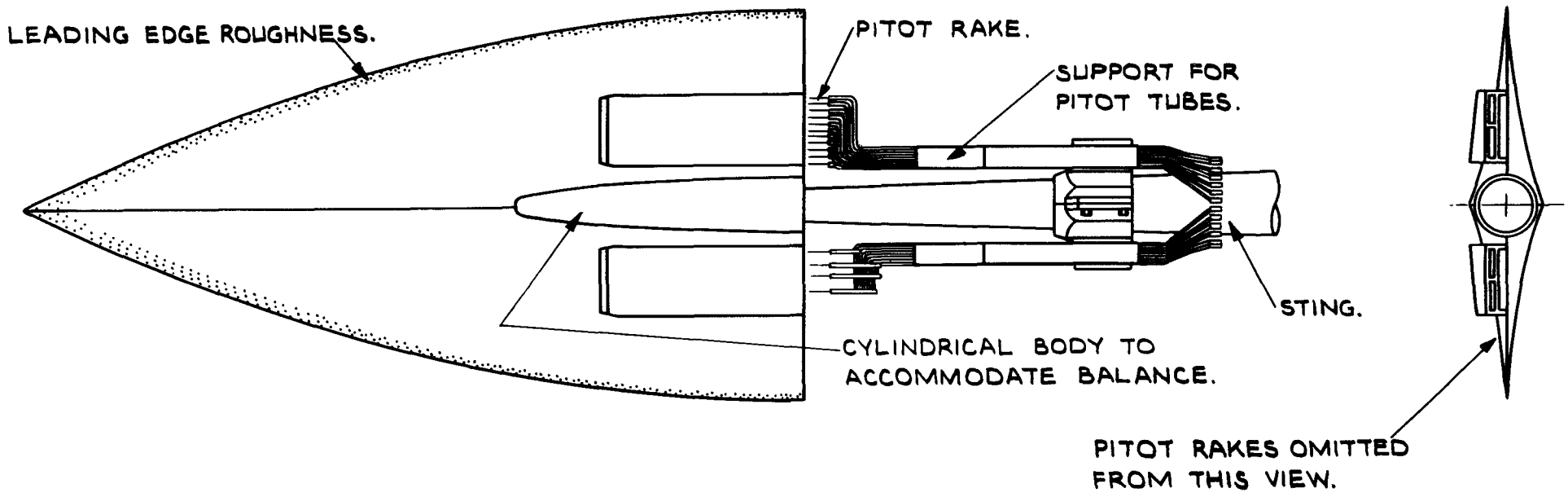

FIG. 10. SKETCH OF MODEL WITH EXIT PITOT RAKES.

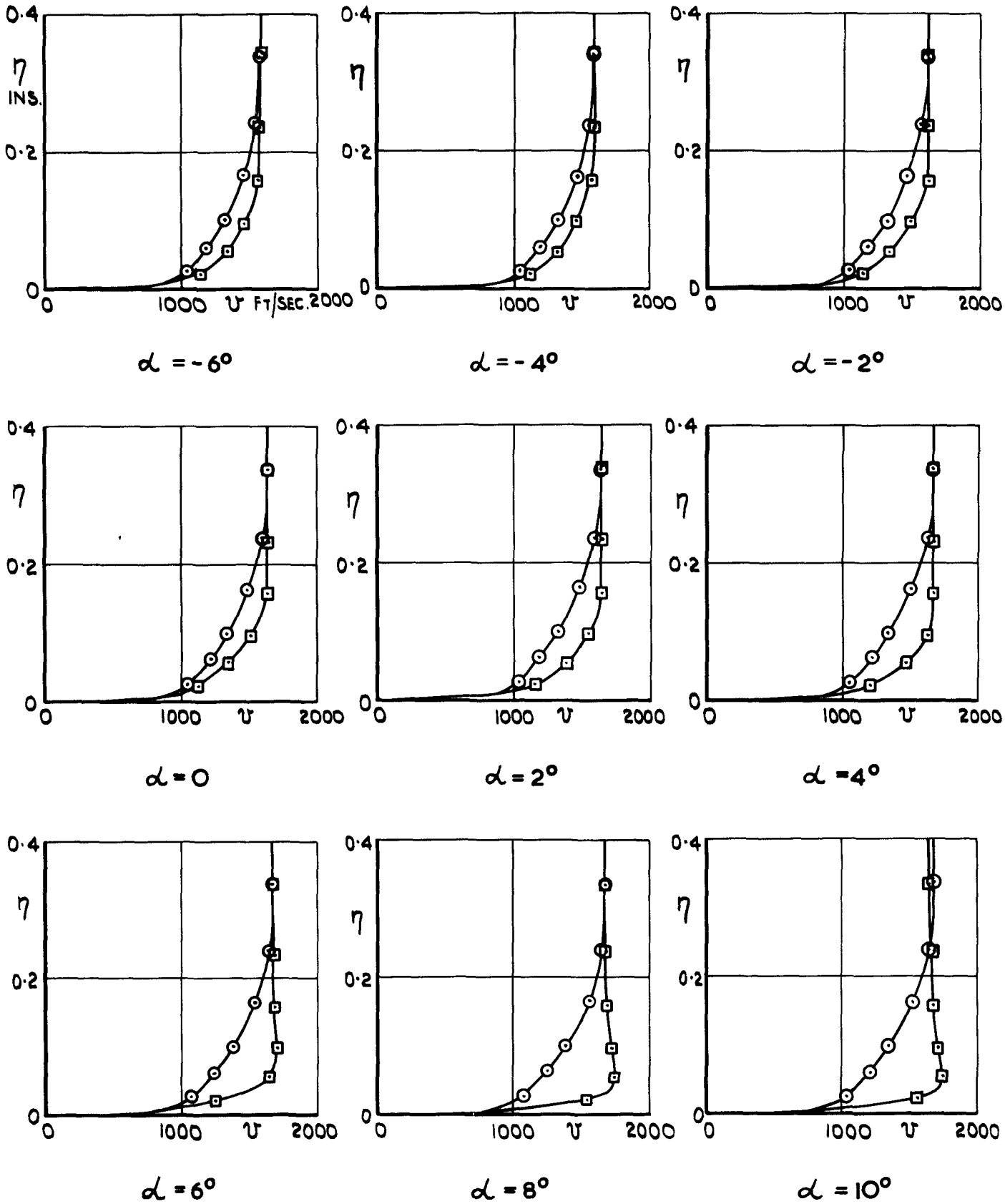

FIG. 11. ENTRY PLANE VELOCITY PROFILES.

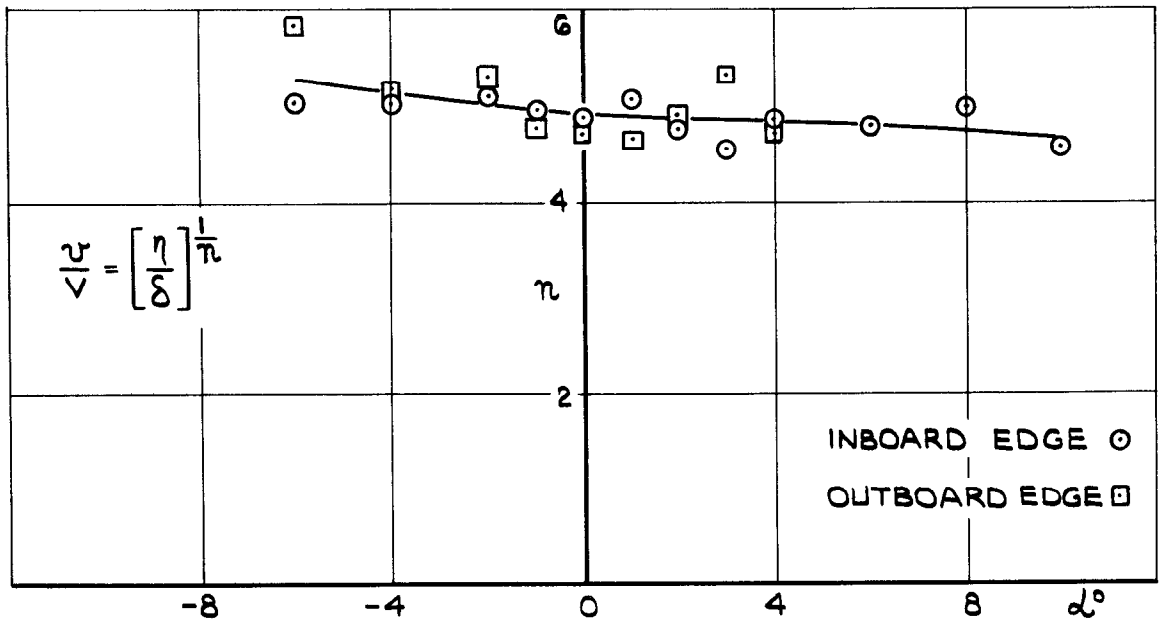

POWER COEFFICIENT n.

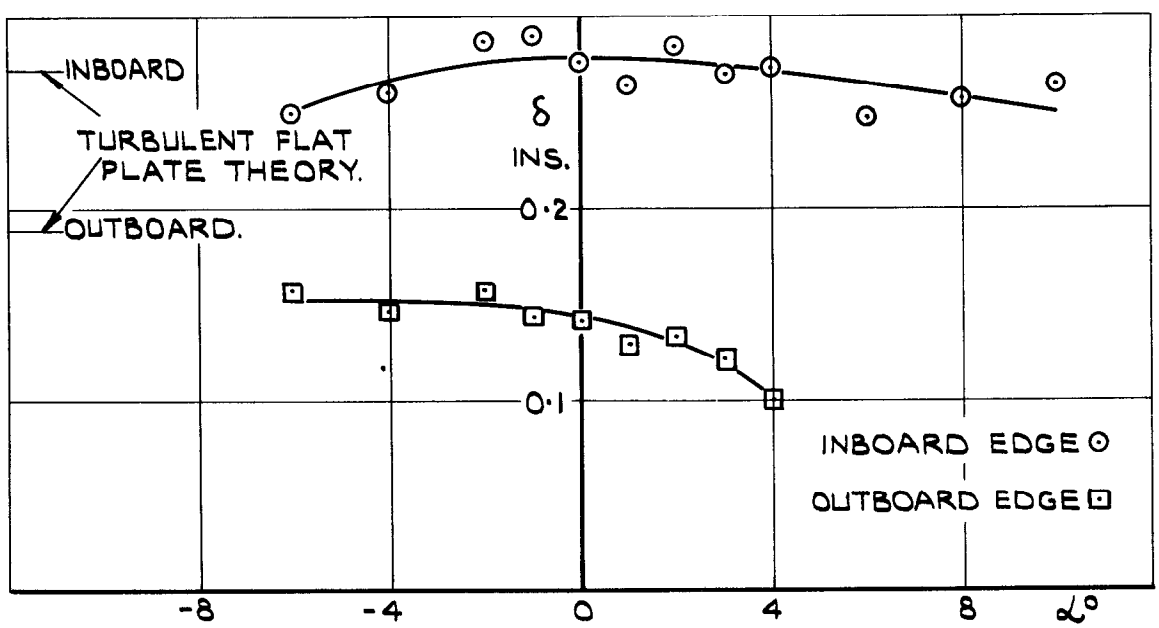

BOUNDARY LAYER THICKNESS δ.

FIG. 12. VARIATION OF PROFILE PARAMETERS WITH INCIDENCE.

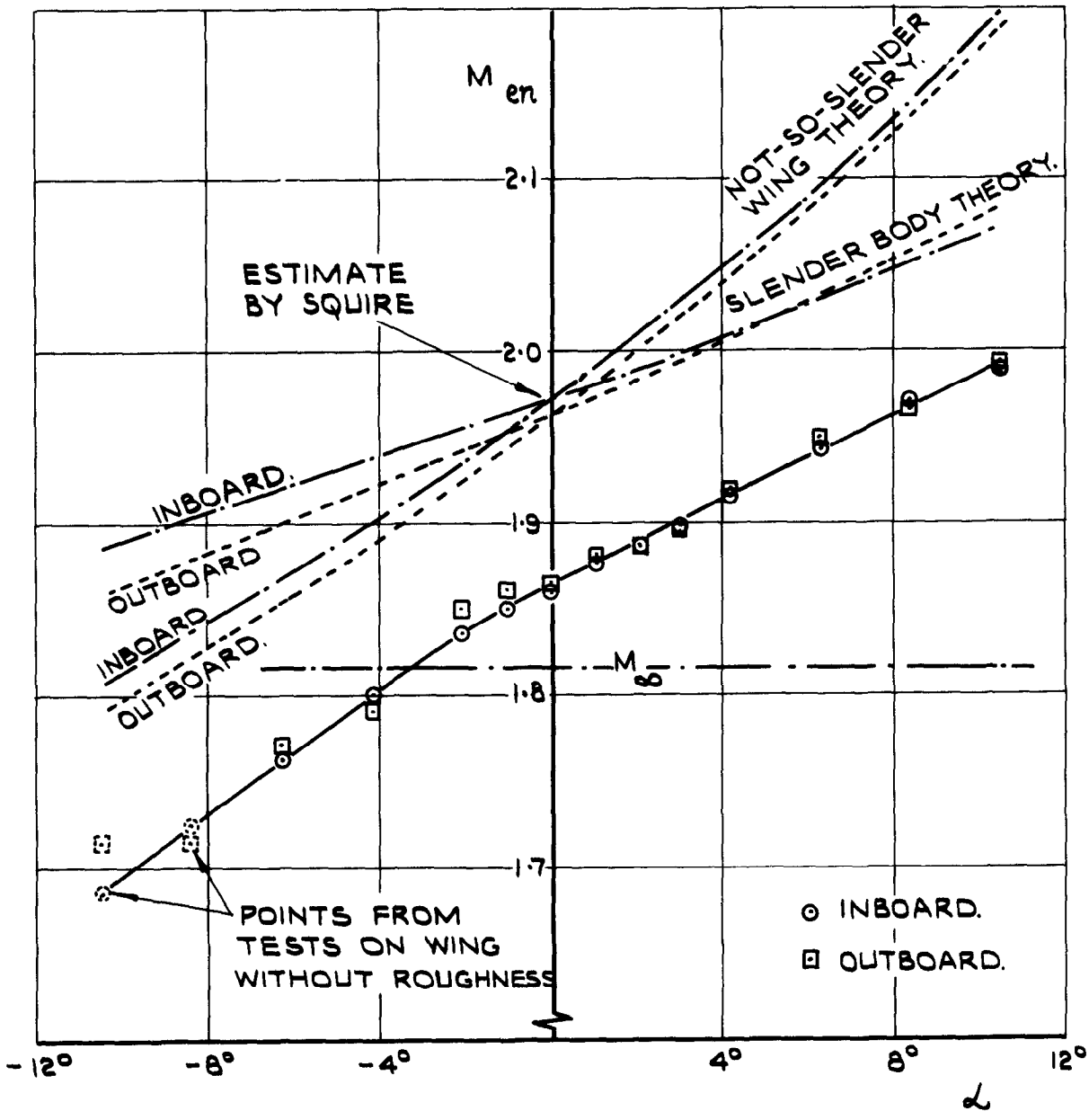

FIG. 13. VARIATION OF ENTRY PLANE MACH No. WITH INCIDENCE.

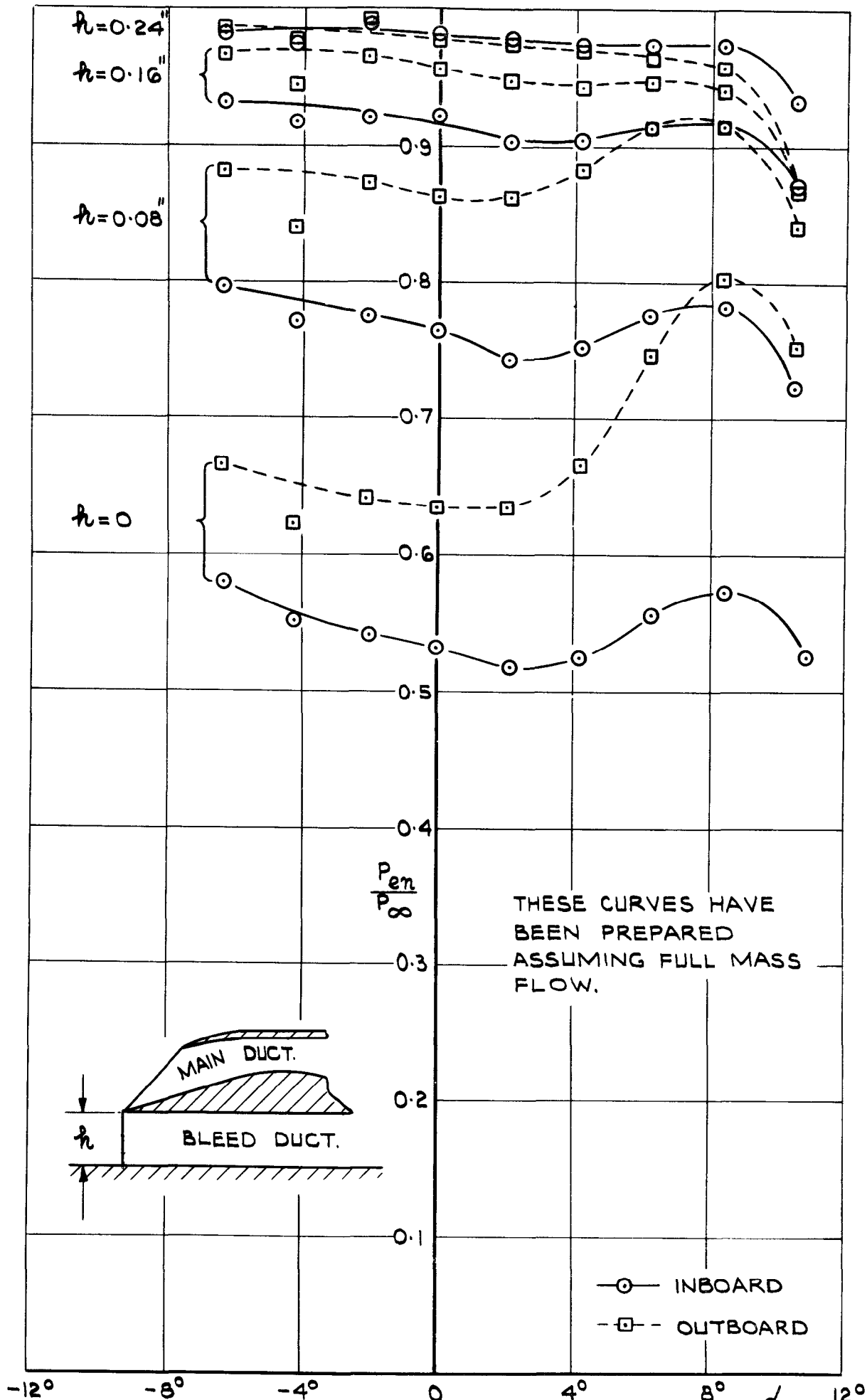

FIG. 14. VARIATION OF MEAN TOTAL PRESSURE ACROSS INLET WITH INCIDENCE.

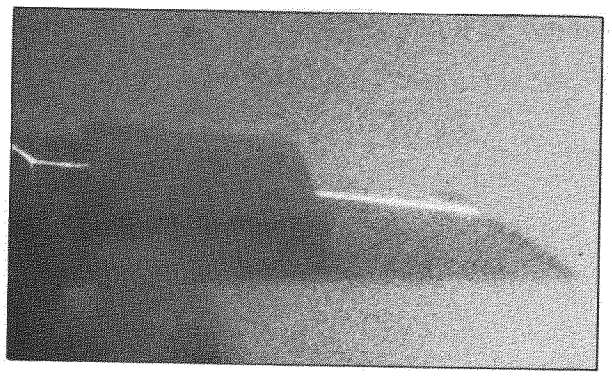

$\alpha = 0$

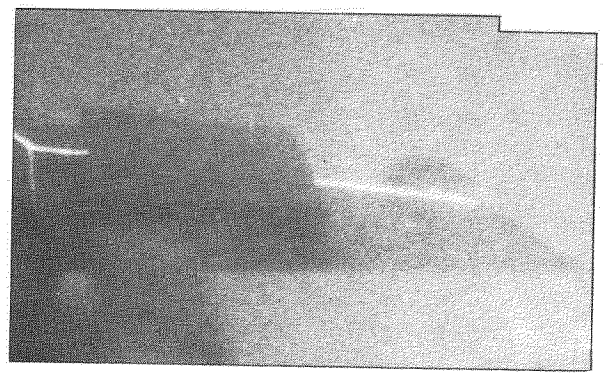

$\alpha = 2{\cdot}1°$

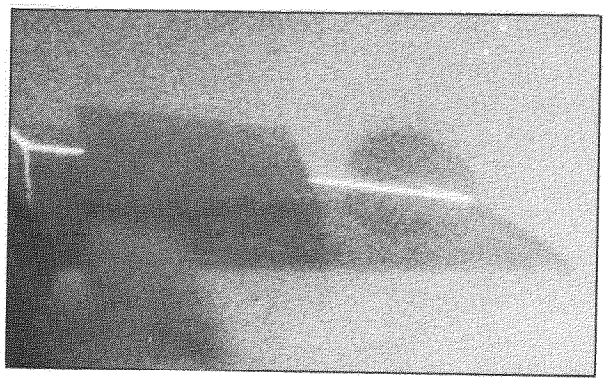

$\alpha = 4{\cdot}2°$

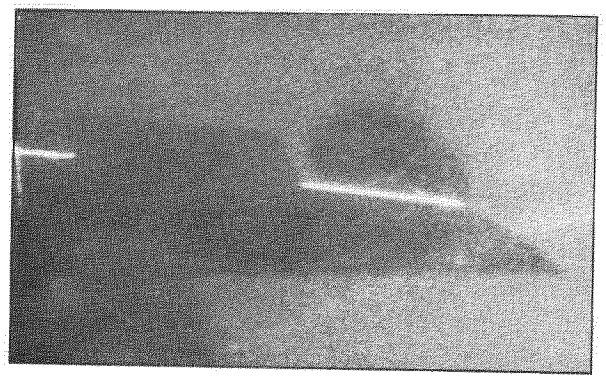

$\alpha = 6{\cdot}3°$

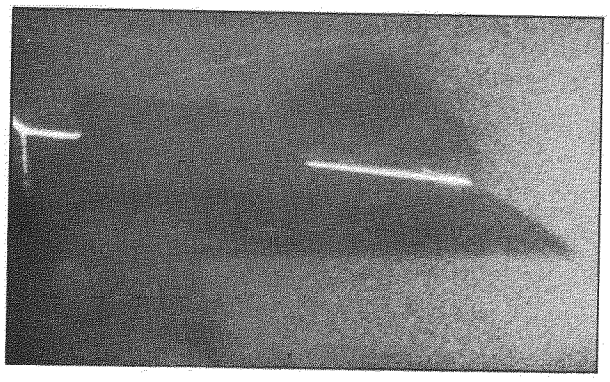

$\alpha = 8{\cdot}4°$

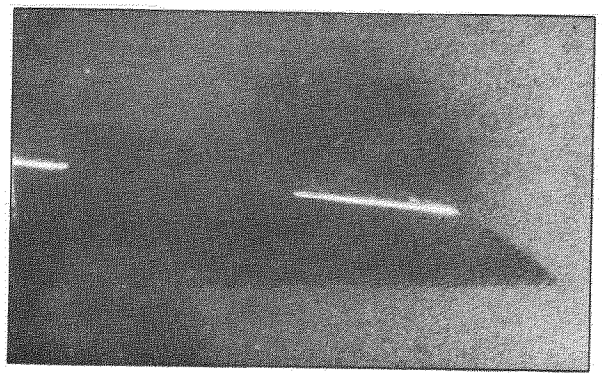

$\alpha = 10{\cdot}5°$

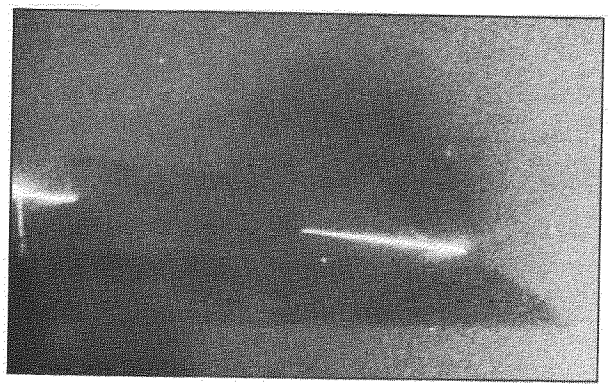

$\alpha = 12{\cdot}7°$

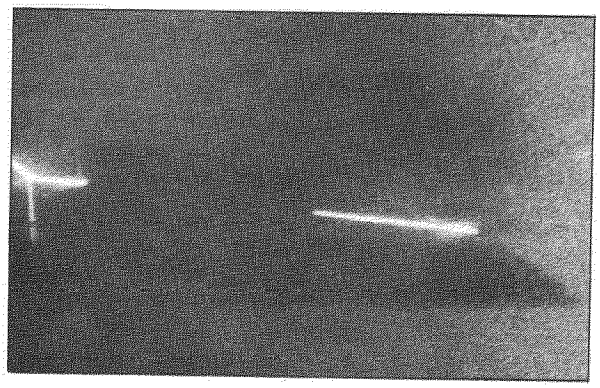

$\alpha = 14{\cdot}8°$

FIG.15. VAPOUR SCREEN PHOTOGRAPHS SHOWING POSITION OF THE WING VORTEX AT THE ENTRY PLANE;

$$h = 0{\cdot}24", \quad \frac{A_{ex}}{A_{en}} = 1{\cdot}02$$

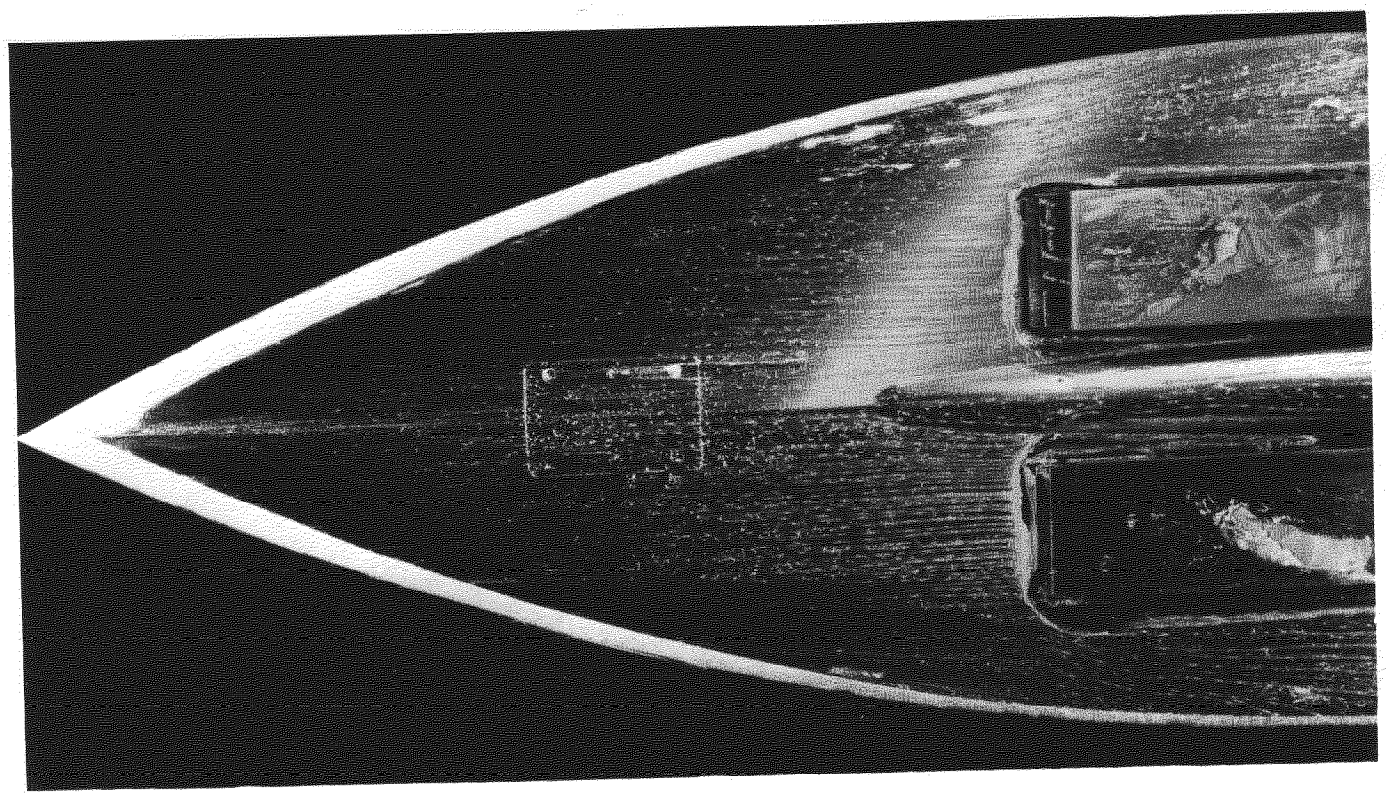

(a) $\alpha = -8{\cdot}4^\circ$

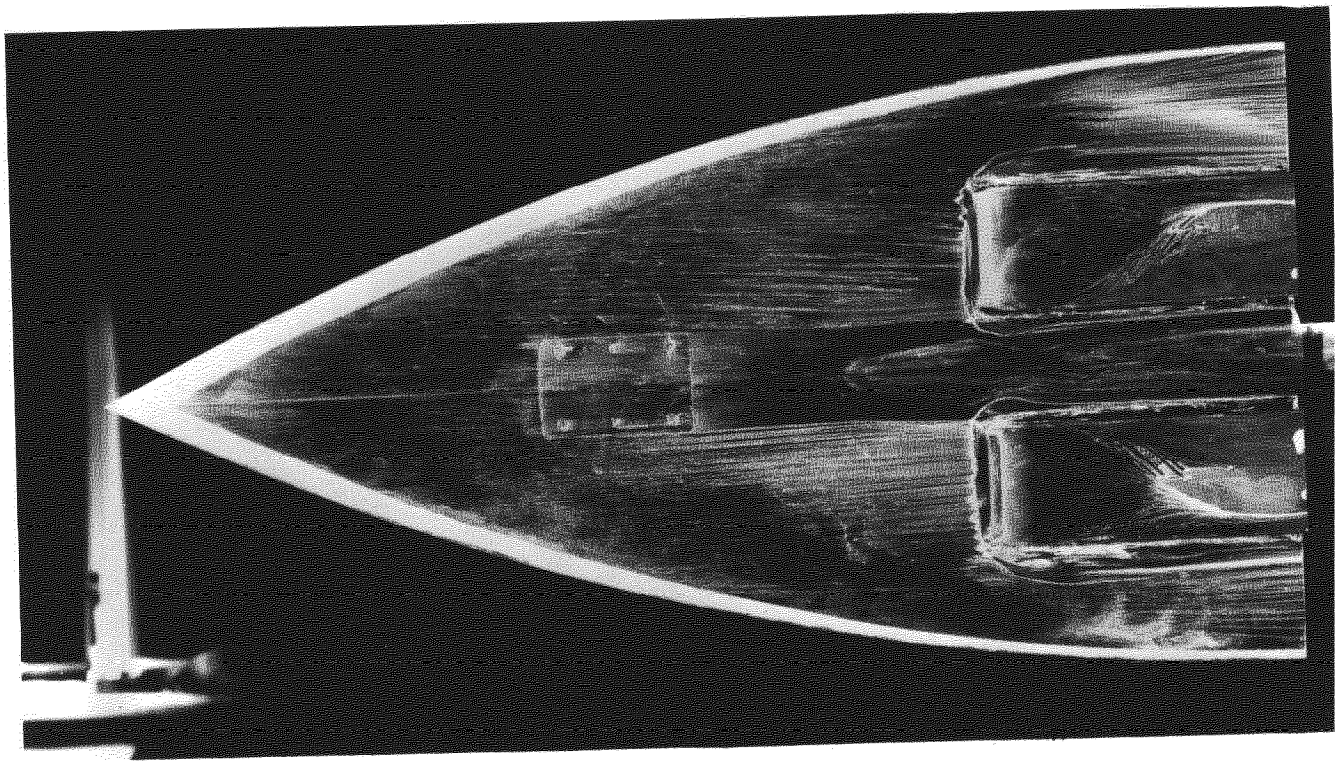

(b) $\alpha = -4{\cdot}2^\circ$

FIG.16a&b. OIL FLOW PHOTOGRAPHS;

$h = 0{\cdot}24"$, $\frac{A_{ex}}{A_{en}} = 1{\cdot}02$ $\alpha = -8{\cdot}4^\circ$ and $-4{\cdot}2^\circ$

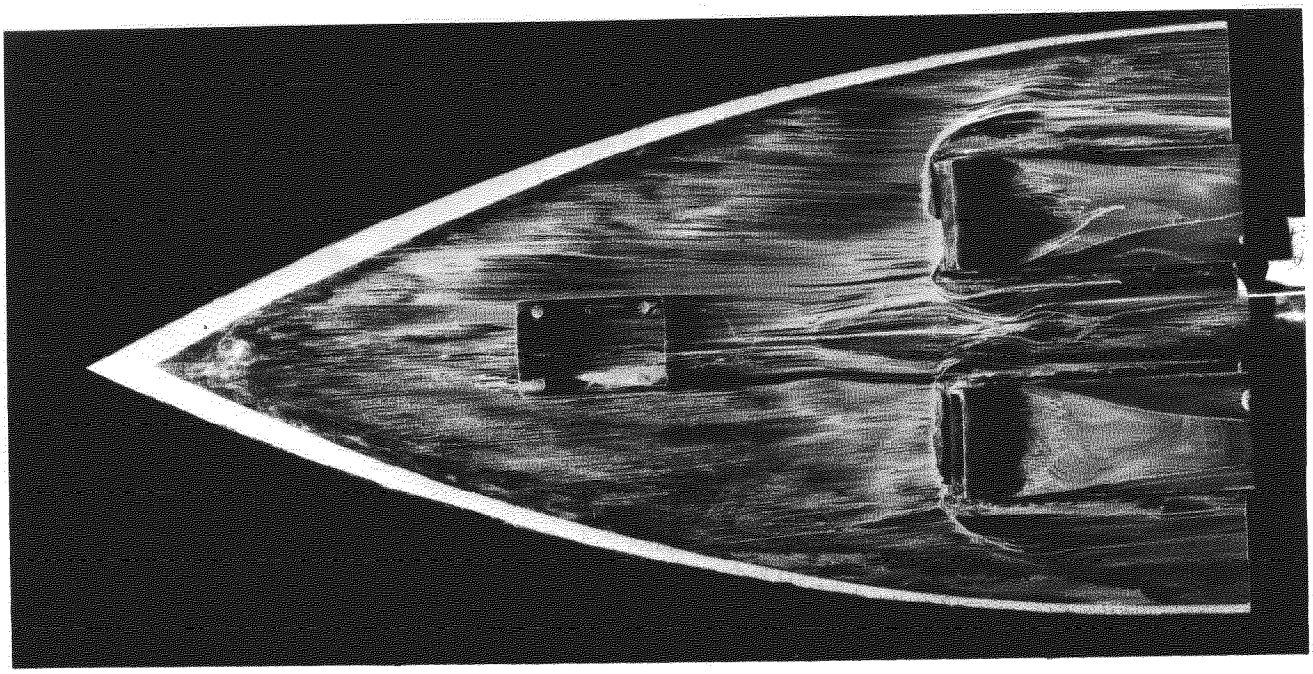

(c) $\alpha = 0$

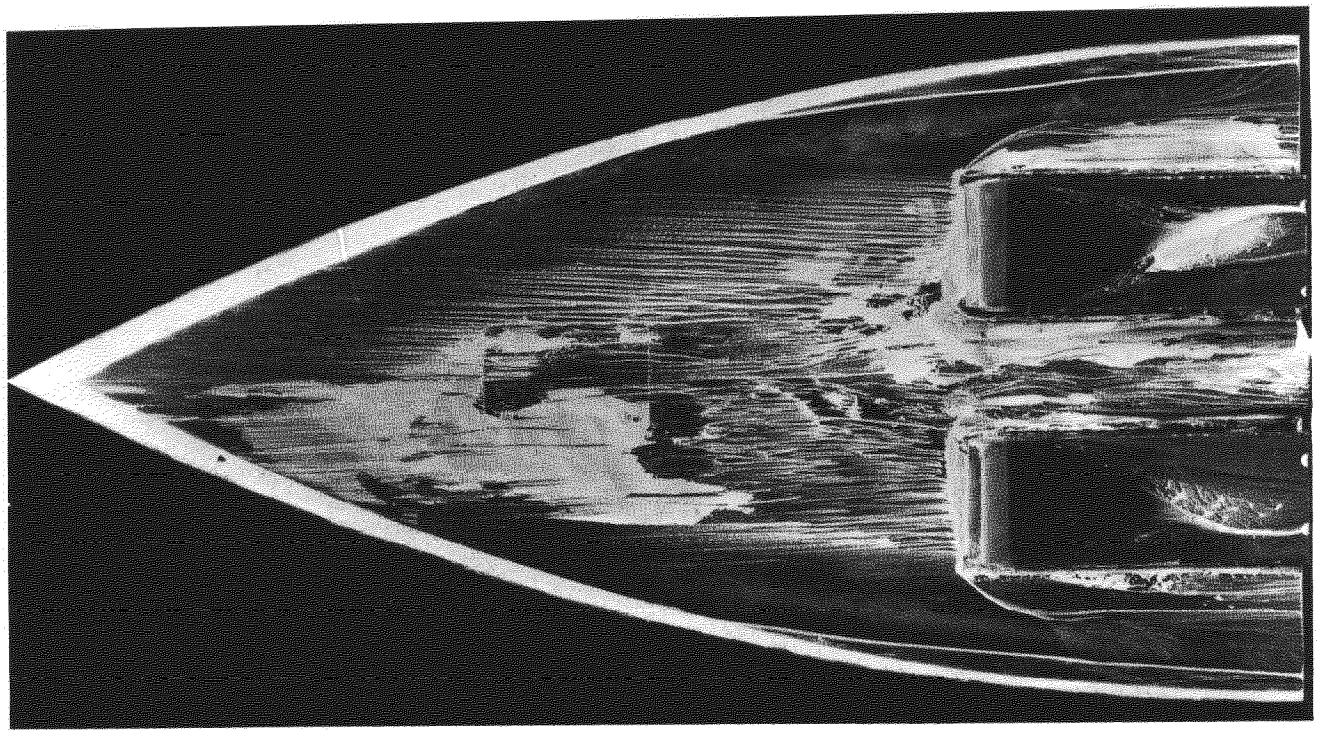

(d) $\alpha = 4{\cdot}2^{\circ}$

FIG.16c&d. OIL FLOW PHOTOGRAPHS;

$h = 0{\cdot}24''$, $\frac{A_{ex}}{A_{en}} = 1{\cdot}02$ $\alpha = 0$ and $4{\cdot}2^{\circ}$

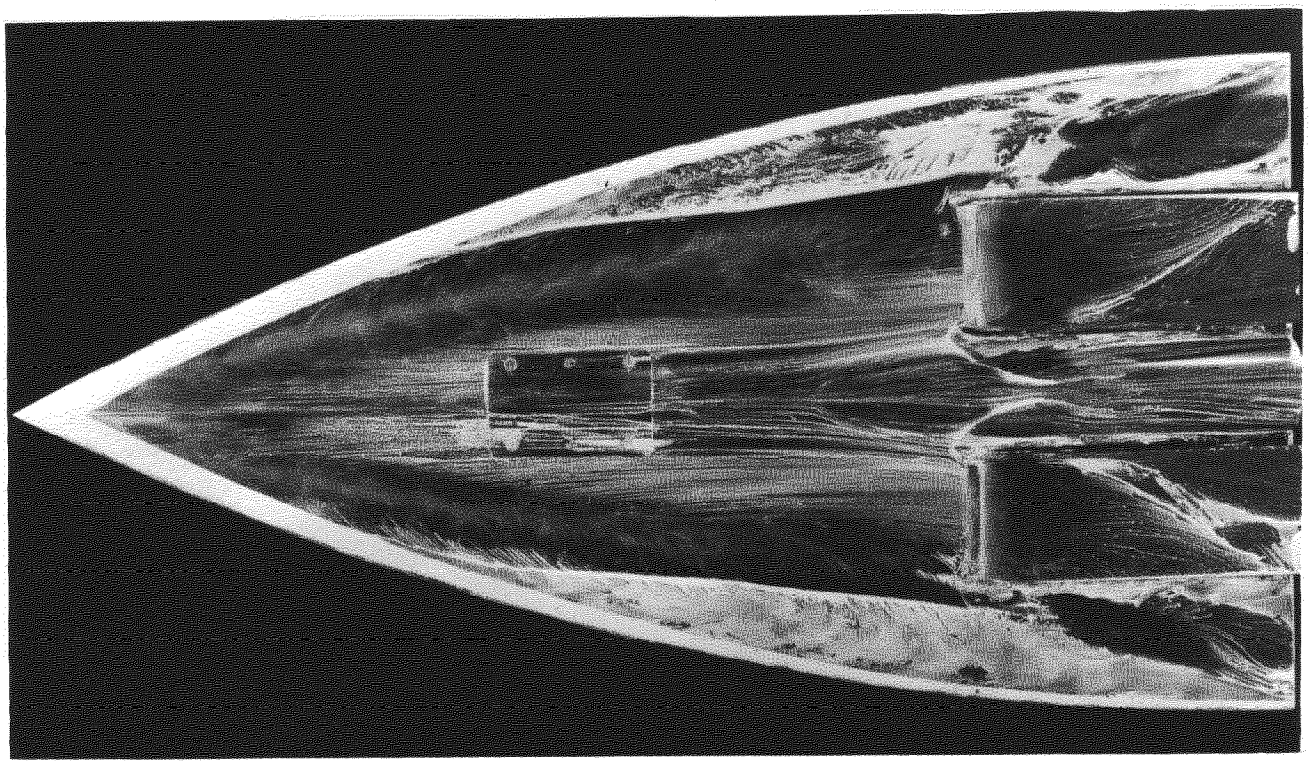

(e) $\alpha = 8{\cdot}4^\circ$

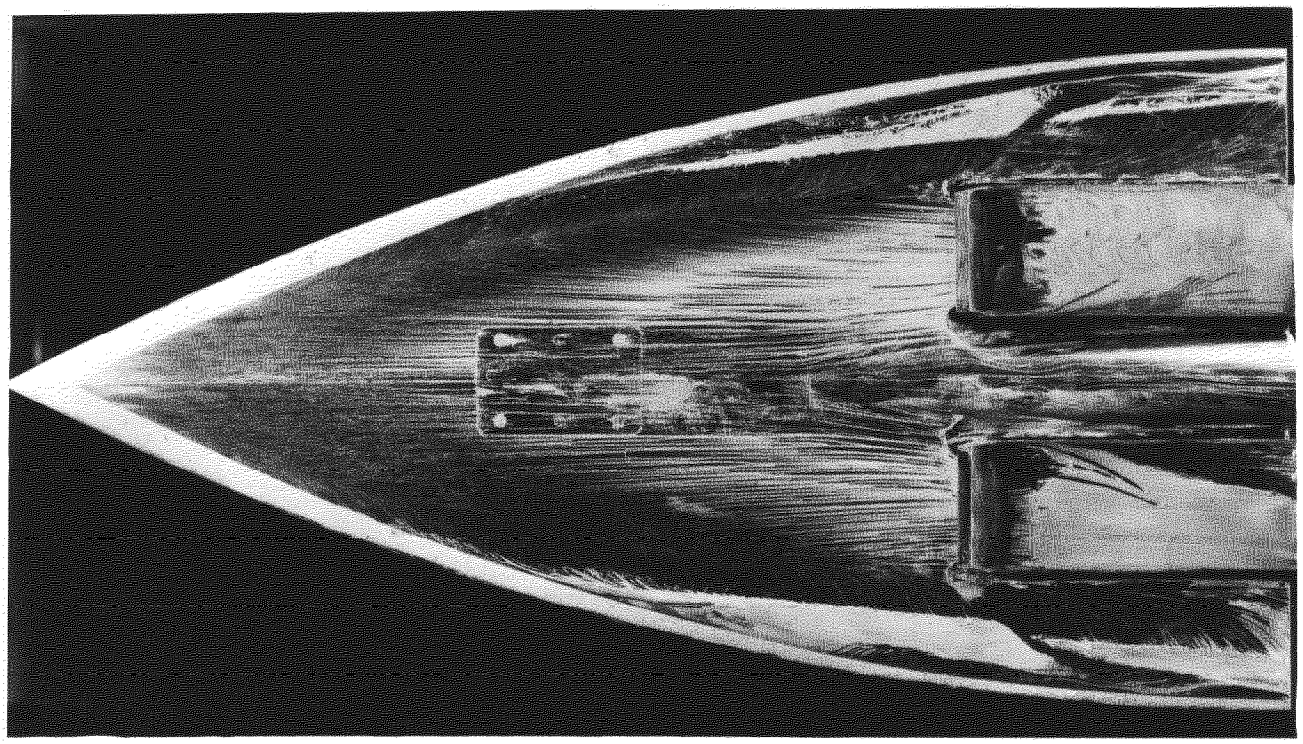

(f) $\alpha = 12{\cdot}7^\circ$

FIG. 16e&f. OIL FLOW PHOTOGRAPHS

$h = 0{\cdot}24''$, $\frac{A_{ex}}{A_{en}} = 1{\cdot}02$ $\alpha = 8{\cdot}4^\circ$ and $12{\cdot}7^\circ$

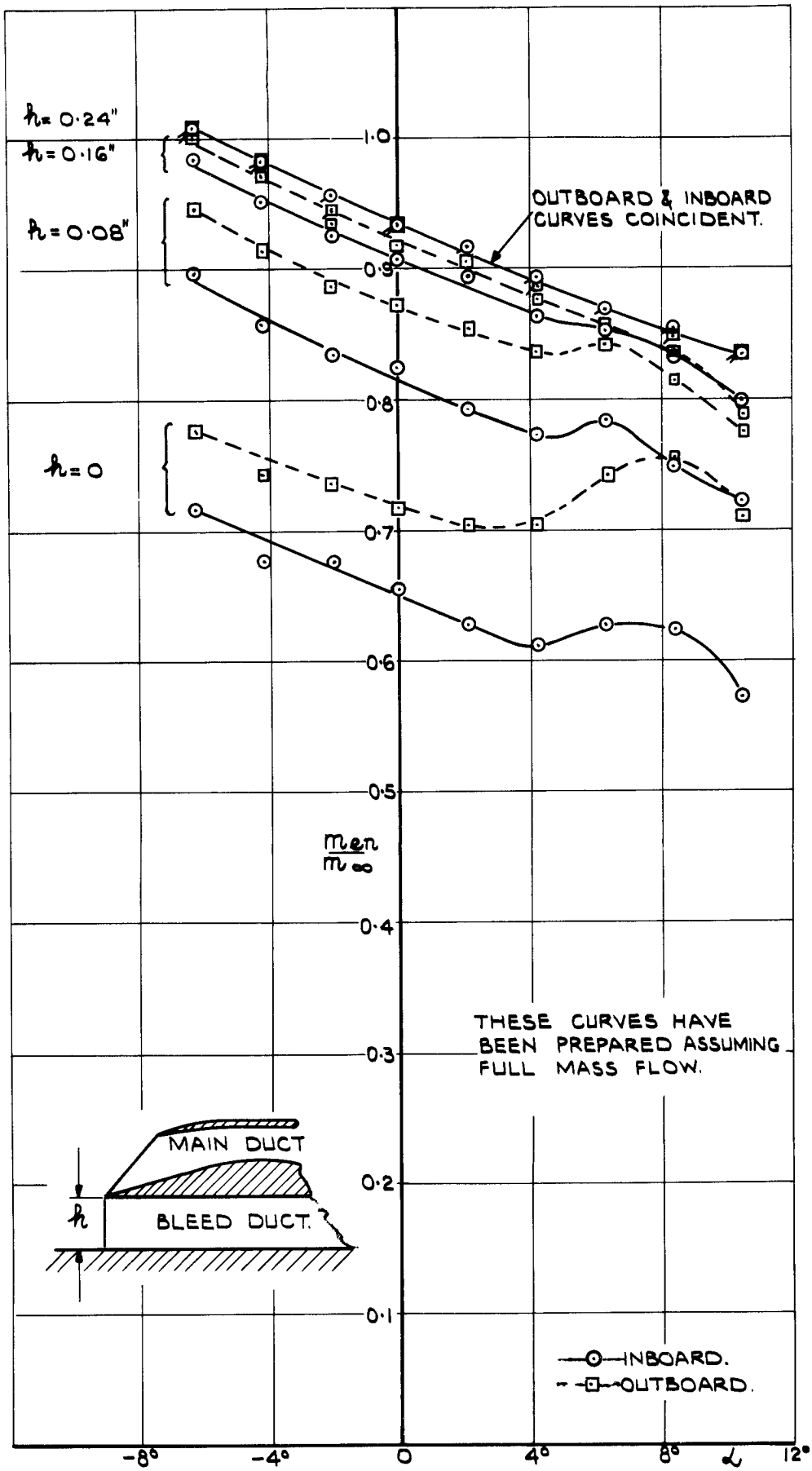

FIG. 17. VARIATION OF MASS FLOW AT ENTRY PLANE WITH INCIDENCE.

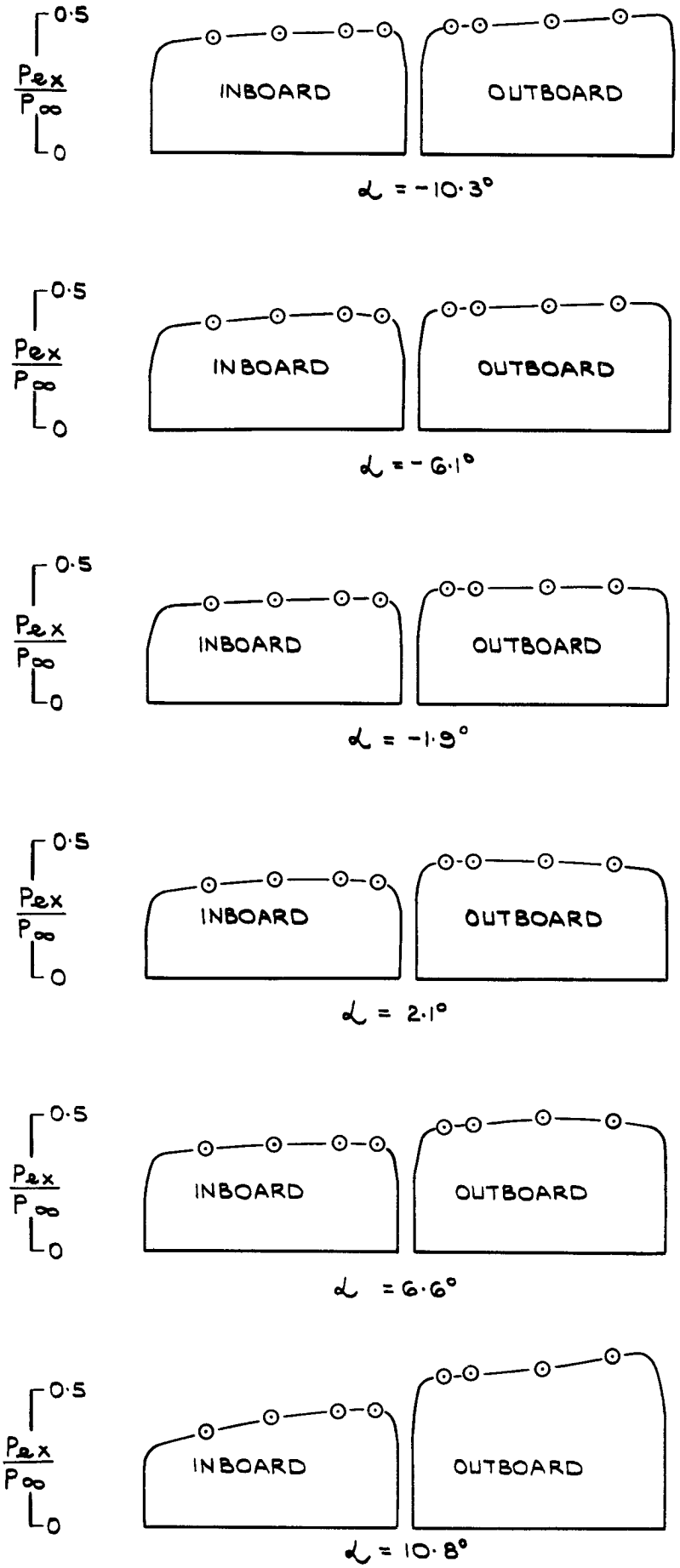

FIG. 18 (a). TOTAL PRESSURE DISTRIBUTION ACROSS HORIZONTAL CENTRE LINE OF EXIT; $\frac{A_{ex}}{A_{en}} = 0.86$; $h = 0$.

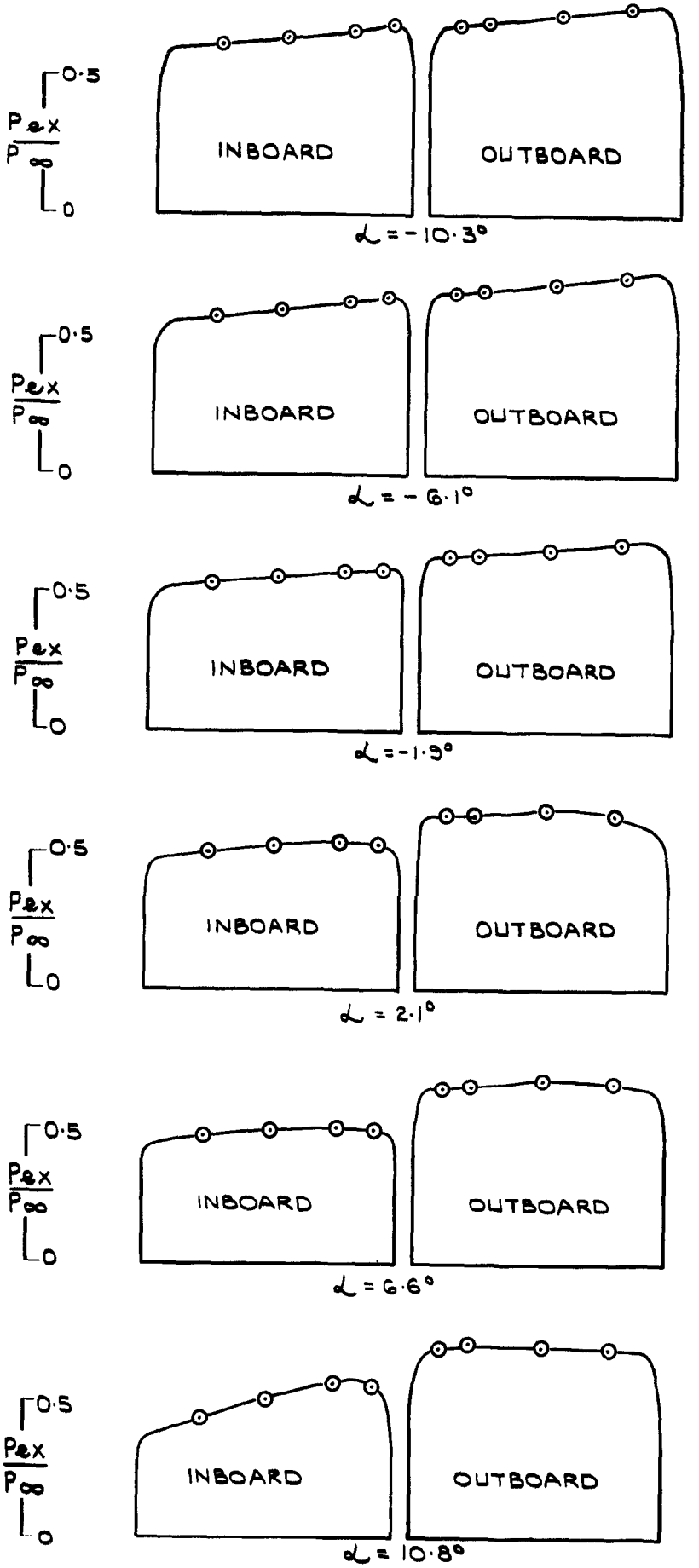

FIG. 18(b) TOTAL PRESSURE DISTRIBUTION ACROSS CENTRE LINE OF EXIT; $\frac{A_{ex}}{A_{en}} = 0{\cdot}86$; $h = 0{\cdot}08''$.

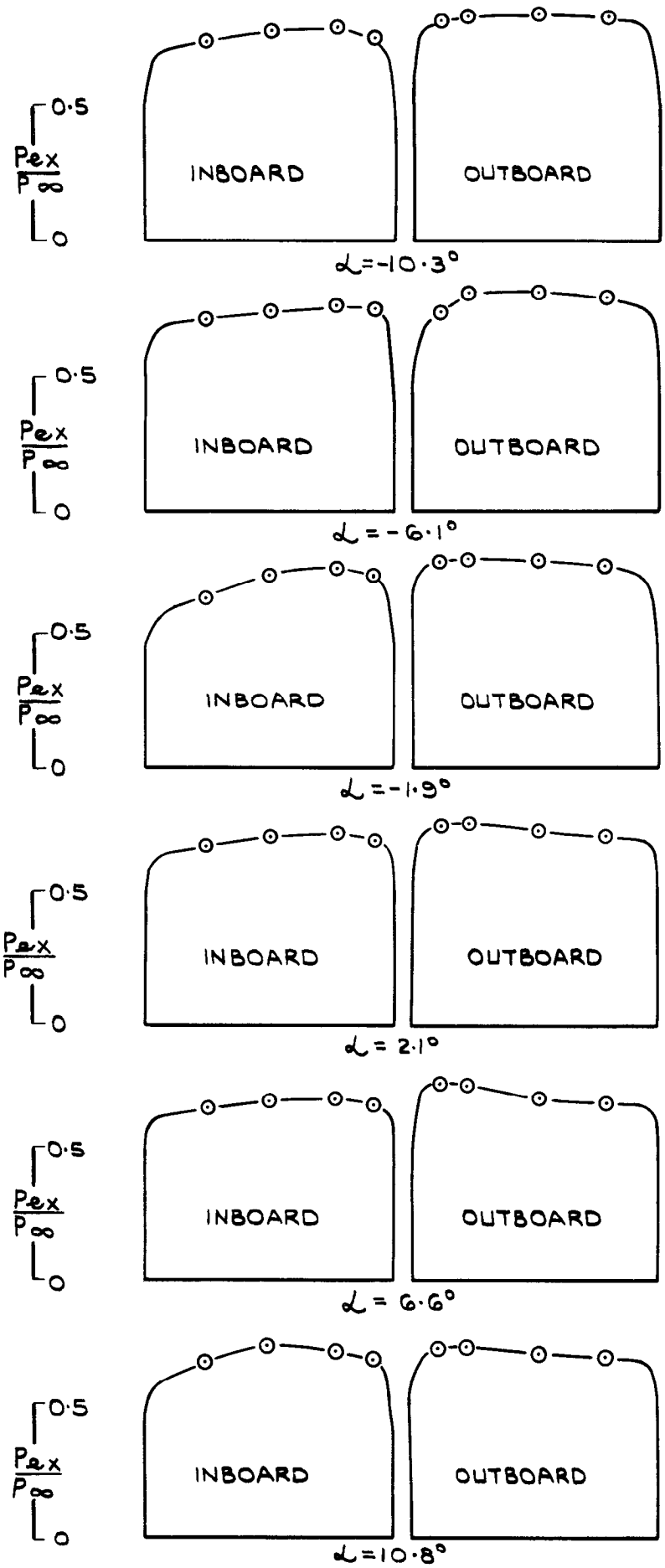

FIG. 18 (c). TOTAL PRESSURE DISTRIBUTION ACROSS CENTRE LINE OF EXIT; $\frac{A_{ex}}{A_{en}} = 0 \cdot 86$; $\frac{\ell}{h} = 0 \cdot 16''$.

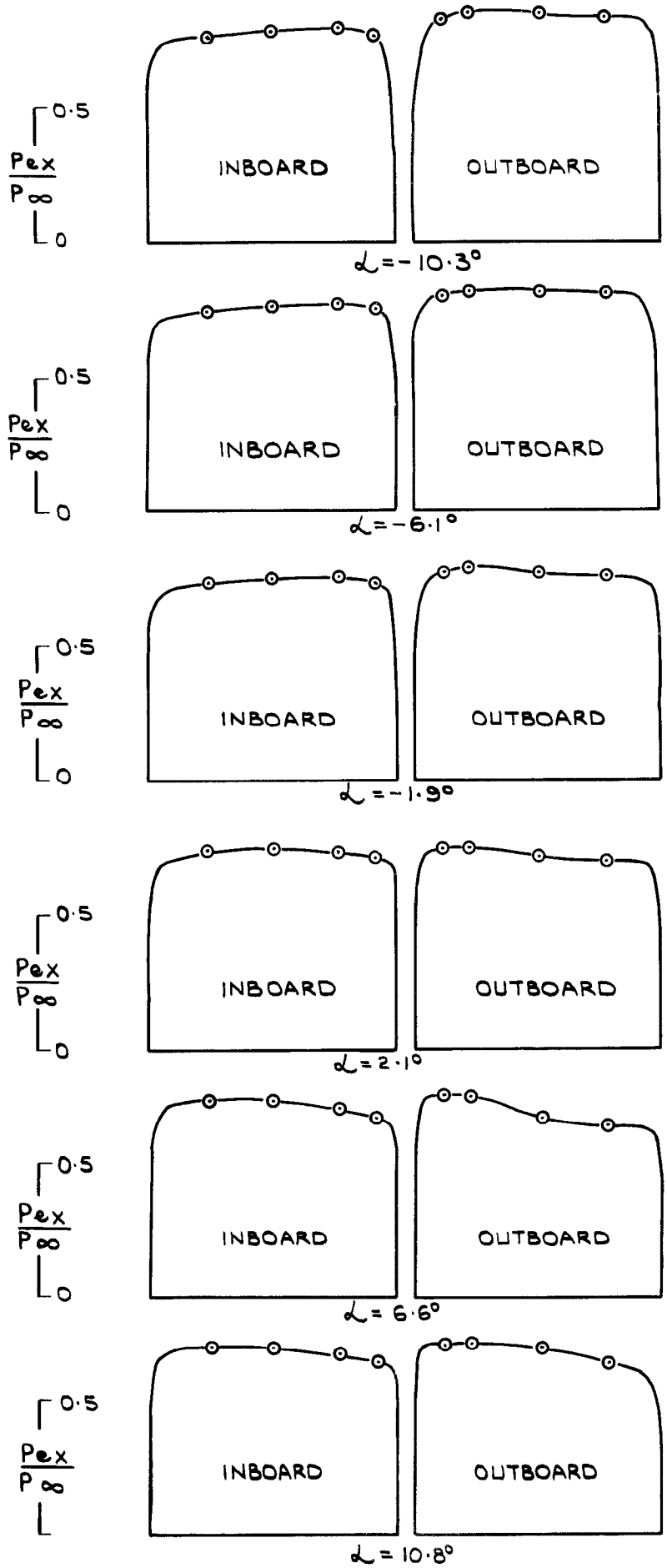

FIG. 18 (d) TOTAL PRESSURE DISTRIBUTION ACROSS CENTRE LINE OF EXIT; $\frac{A_{ex}}{A_{en}} = 0 \cdot 86$; $h = 0 \cdot 24''$.

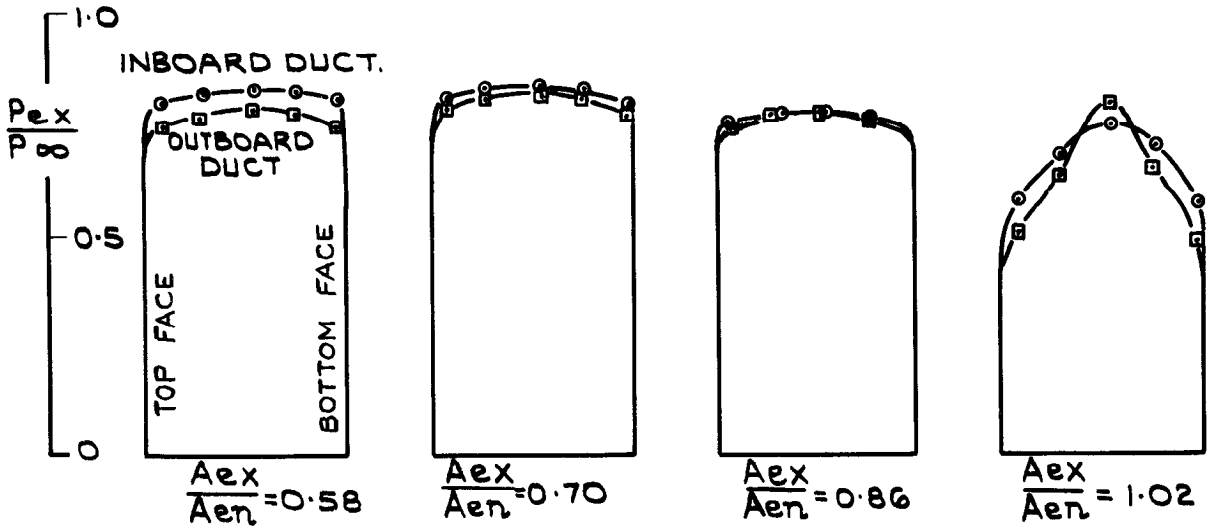

(a) VARIATION WITH EXIT AREA; $\alpha = 0$; $h = 0{\cdot}24''$.

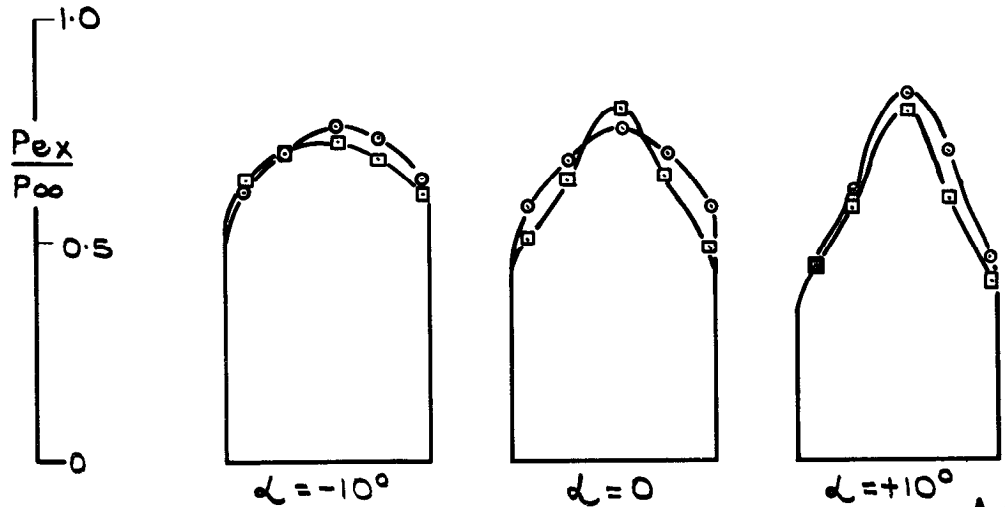

(b) VARIATION WITH INCIDENCE; $h = 0{\cdot}24''$; $\frac{Aex}{Aen} = 1{\cdot}02$.

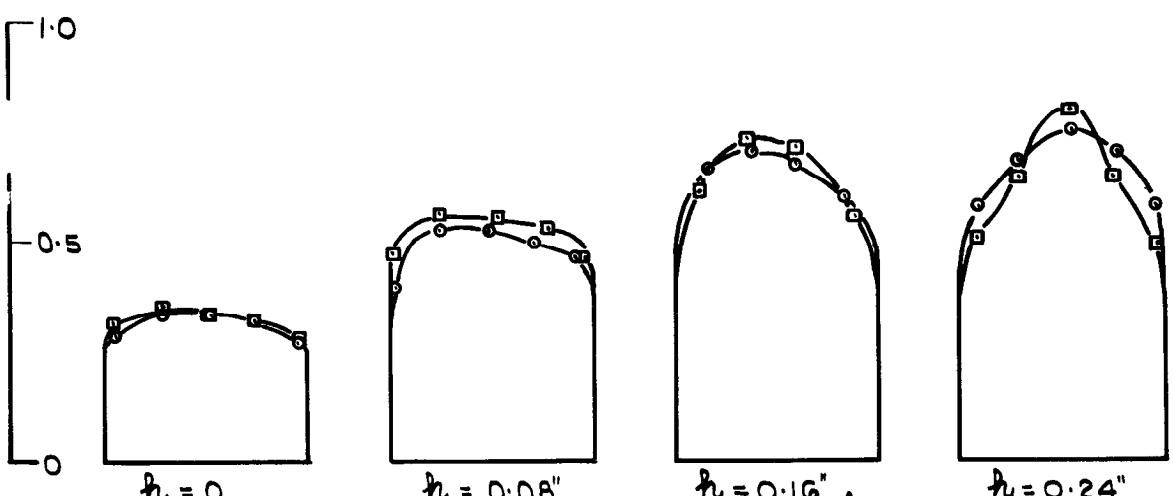

(c) VARIATION WITH BLEED HEIGHT; $\frac{Aex}{Aen} = 1{\cdot}02$; $\alpha = 0$.

FIG. 19. TOTAL PRESSURE DISTRIBUTION ACROSS HEIGHT OF EXIT (SEE FIG. 7 (a)).

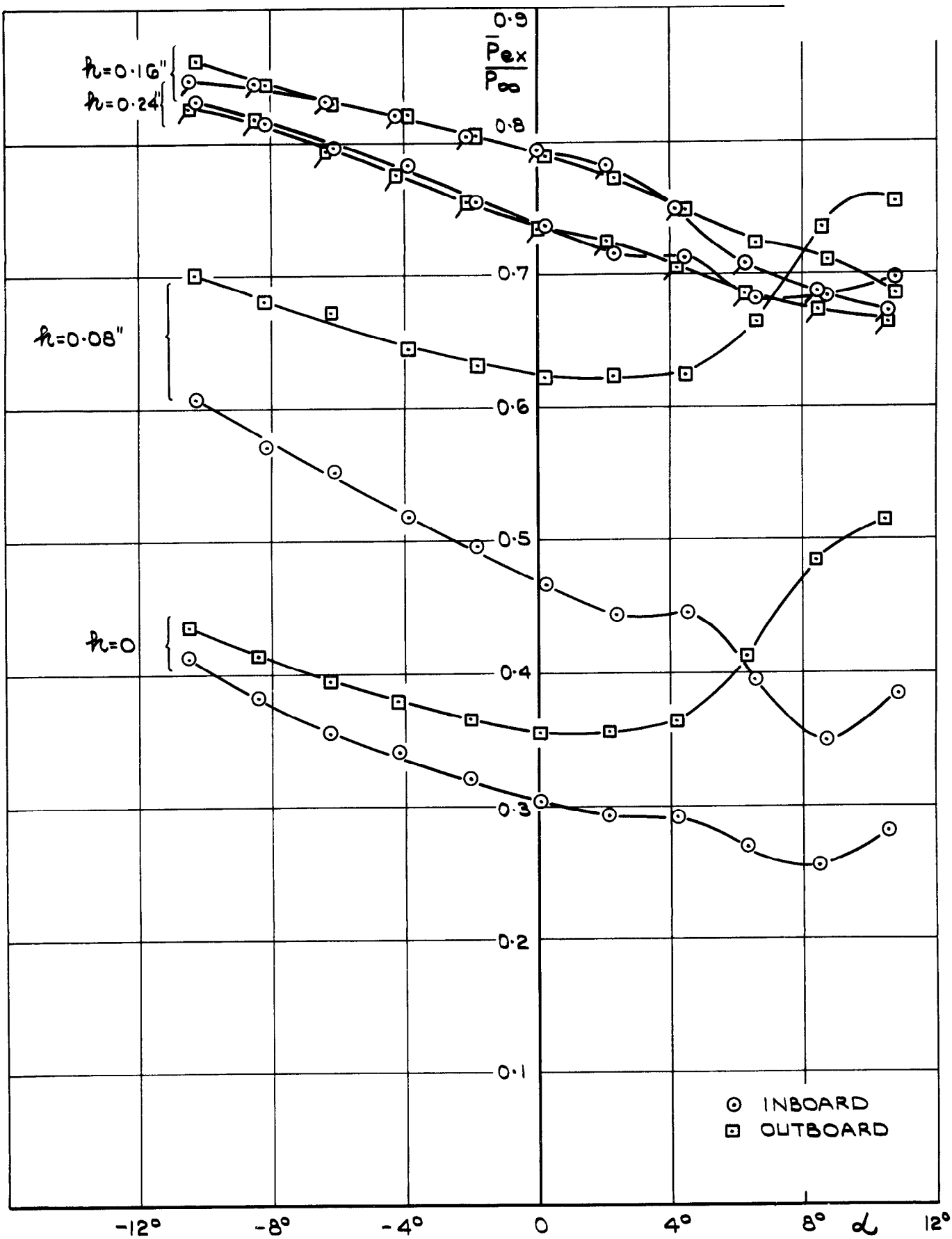

FIG. 20(a) VARIATION OF PRESSURE RECOVERY WITH INCIDENCE FOR $\frac{Aex}{Aen}$ = 0·58.

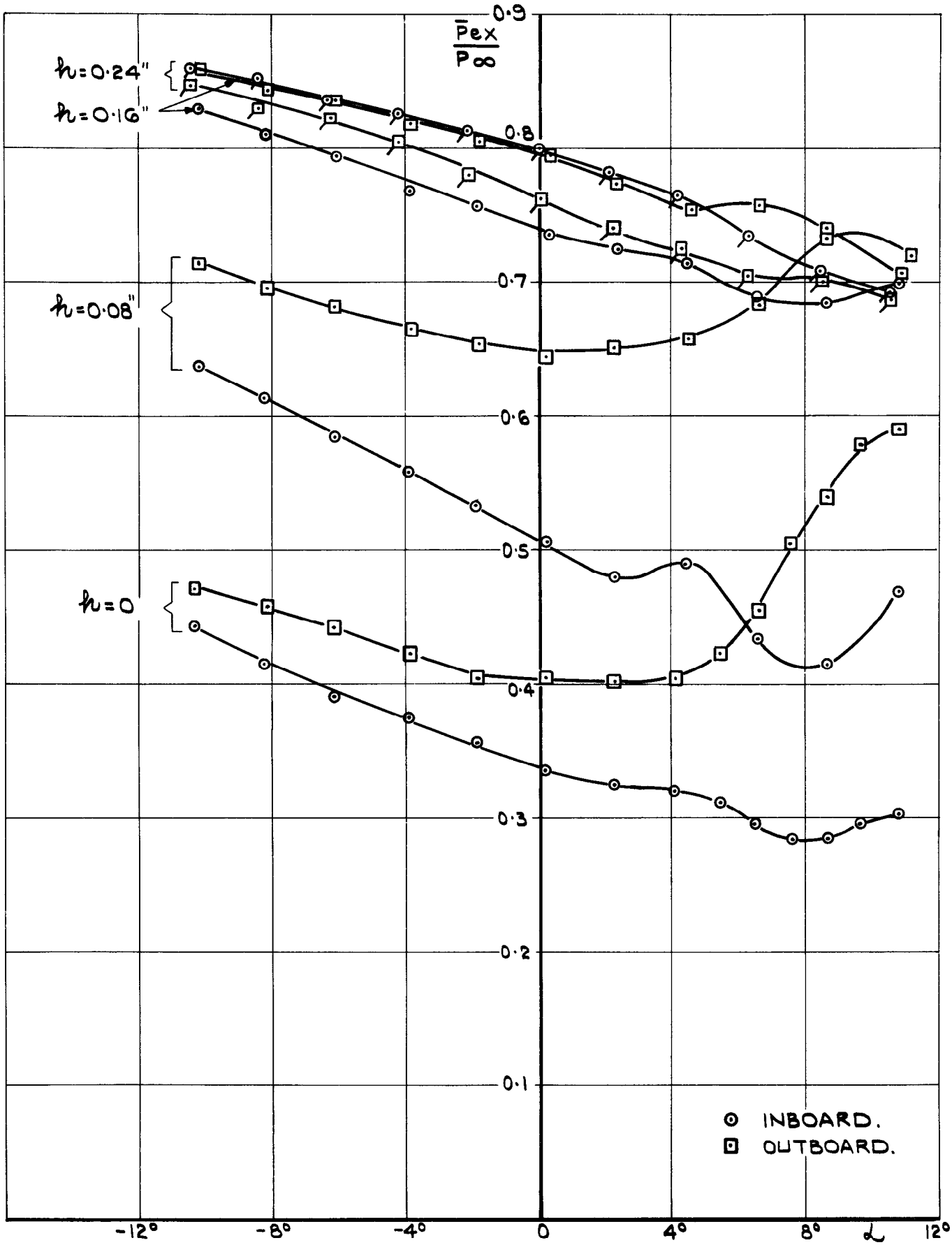

FIG. 20 (b). VARIATION OF PRESSURE RECOVERY WITH INCIDENCE FOR $\frac{Aex}{Aen}$ = 0·70.

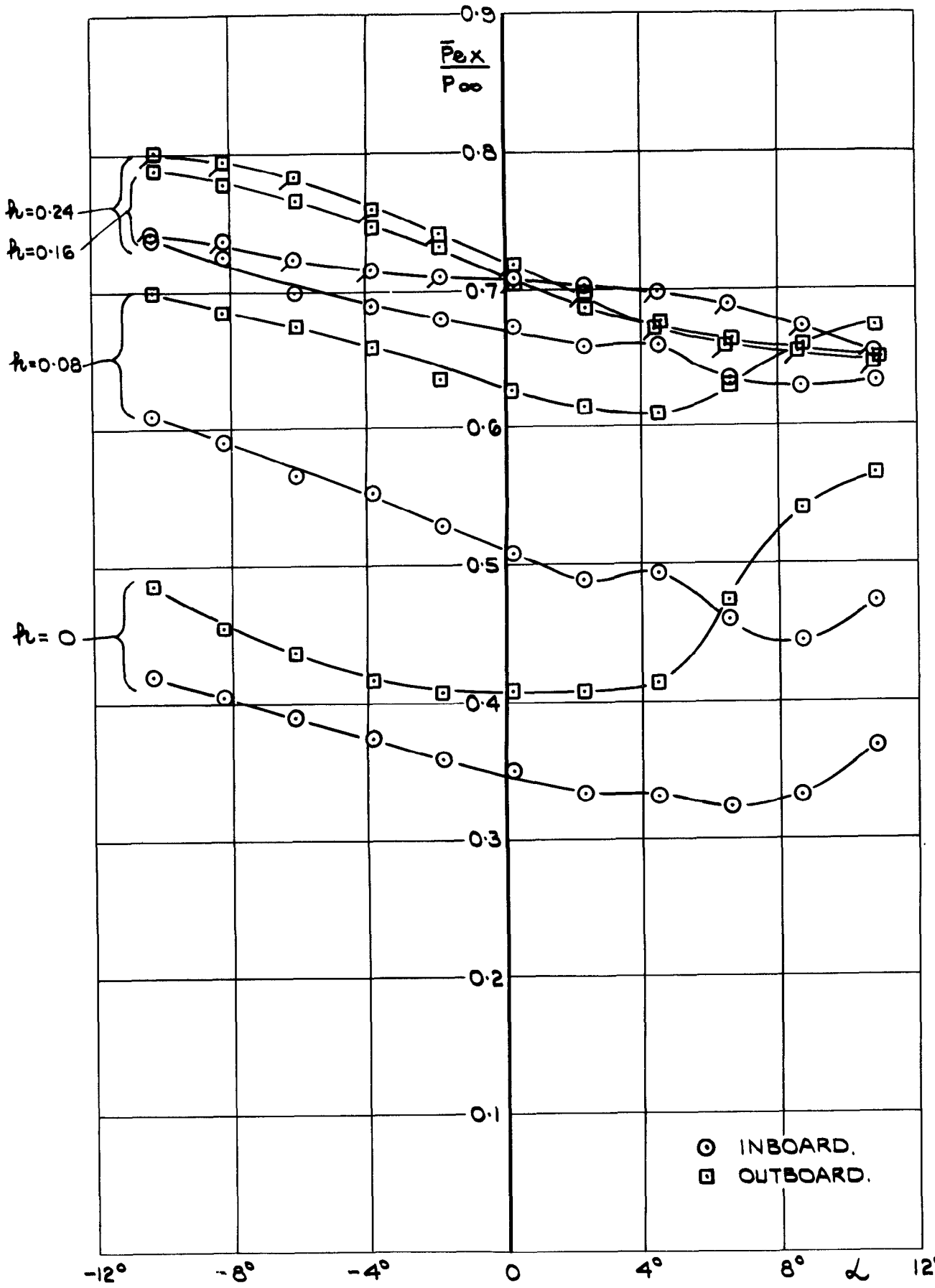

FIG. 20 (c). VARIATION OF PRESSURE RECOVERY WITH INCIDENCE FOR $\frac{Aex}{Aen} = 0{\cdot}86$.

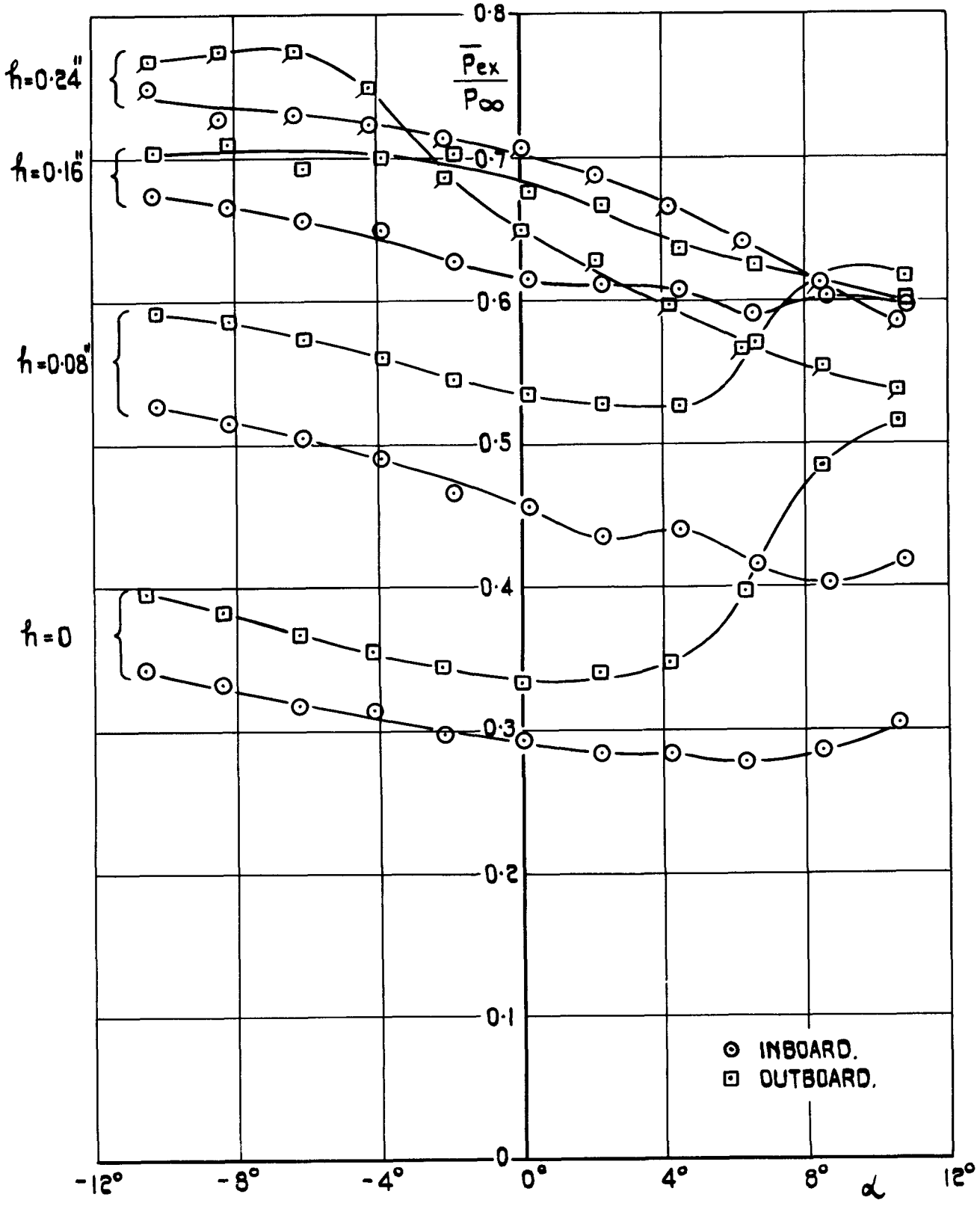

FIG. 20 (d). VARIATION OF PRESSURE RECOVERY WITH INCIDENCE FOR $\frac{Aex}{Aen} = 1{\cdot}02$.

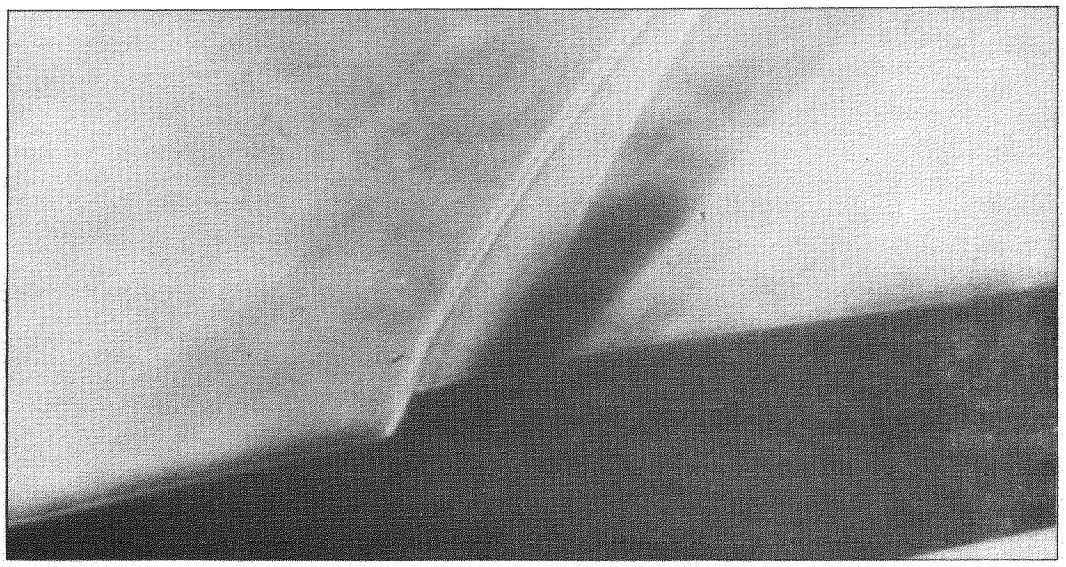

$\alpha = -10°$

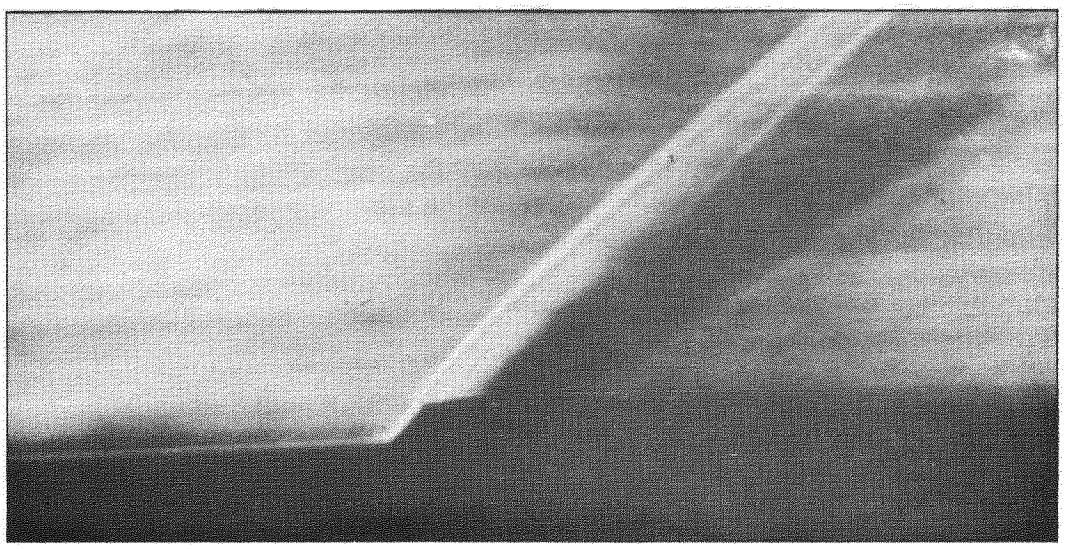

$\alpha = 0$

$\alpha = +10°$

FIG.21. SCHLIEREN PHOTOGRAPHS;

$h = 0{\cdot}24"$; $\frac{A_{ex}}{A_{en}} = 1{\cdot}02$

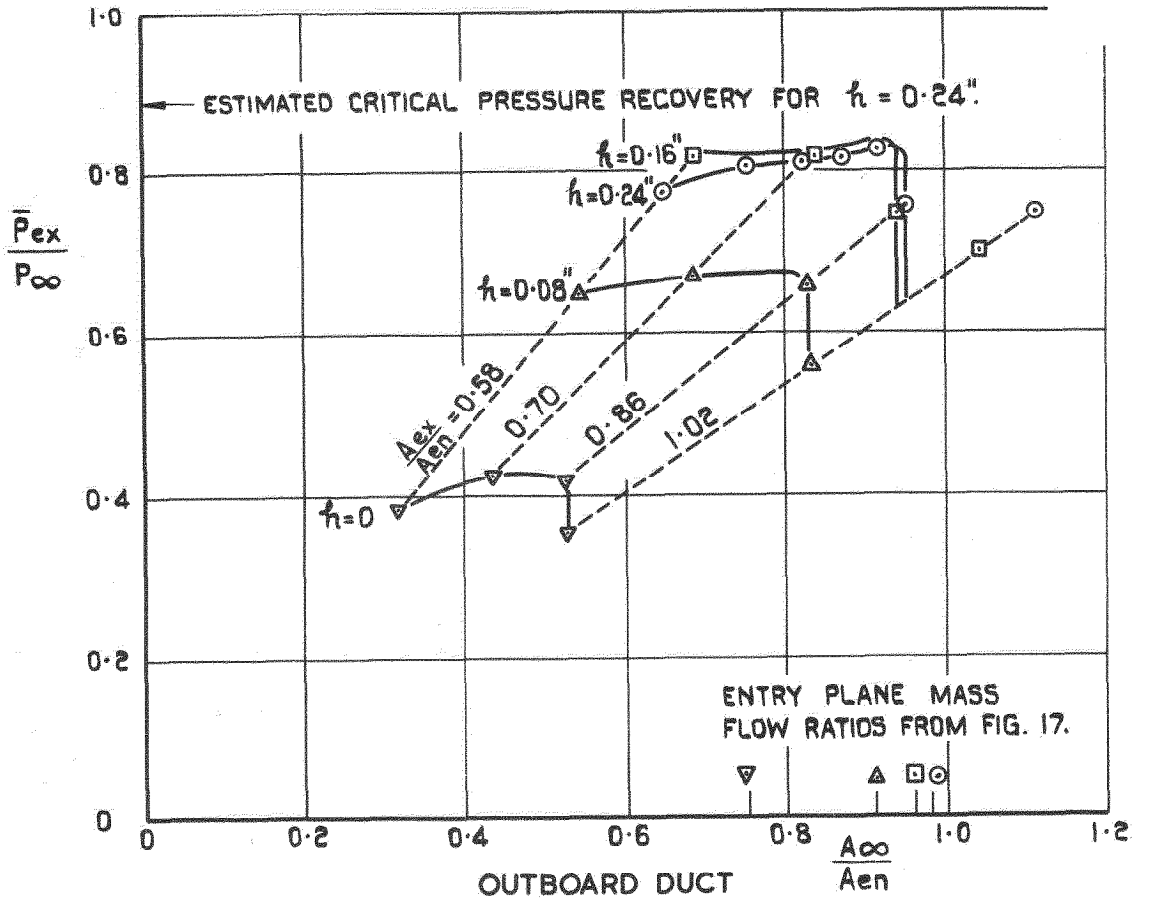

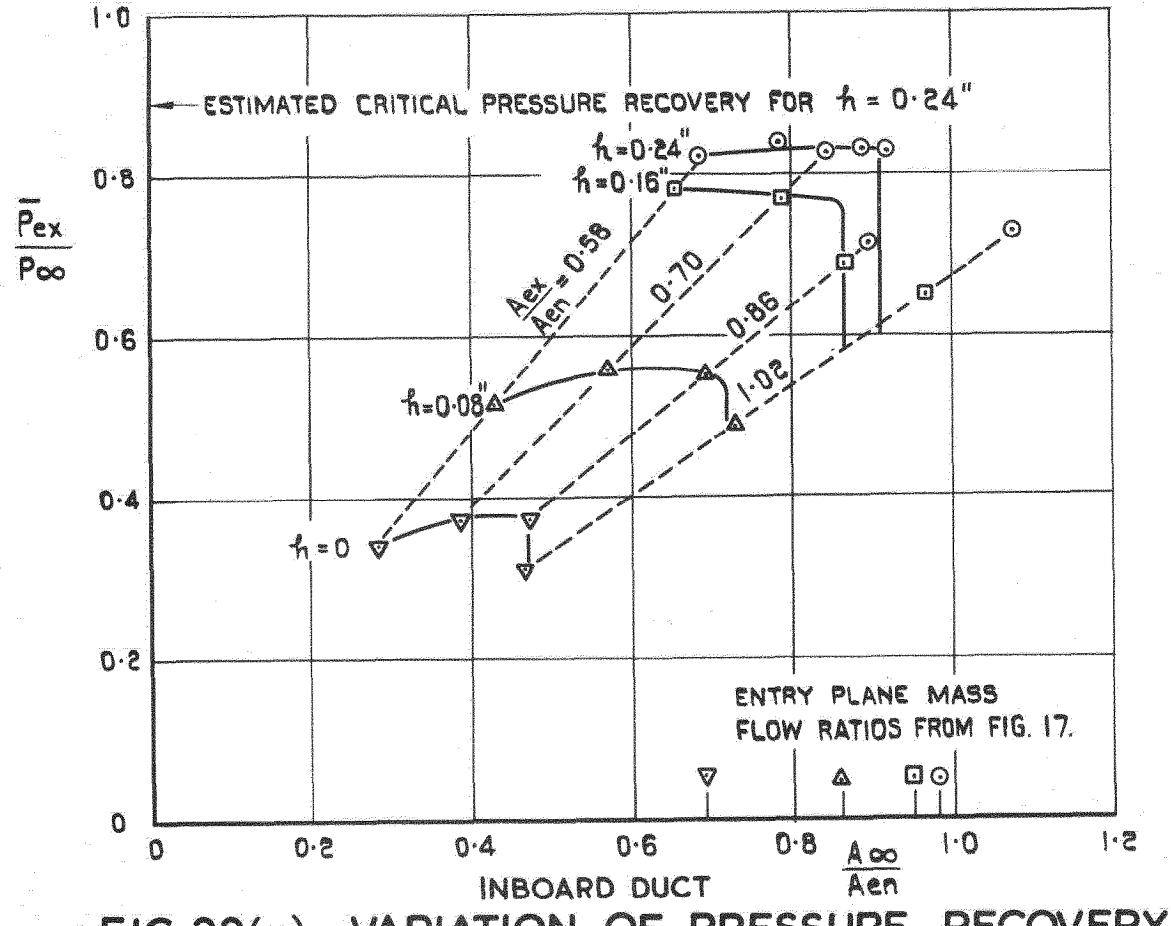

FIG. 22(a). VARIATION OF PRESSURE RECOVERY WITH MASS FLOW RATIO FOR $\alpha = -4°$.

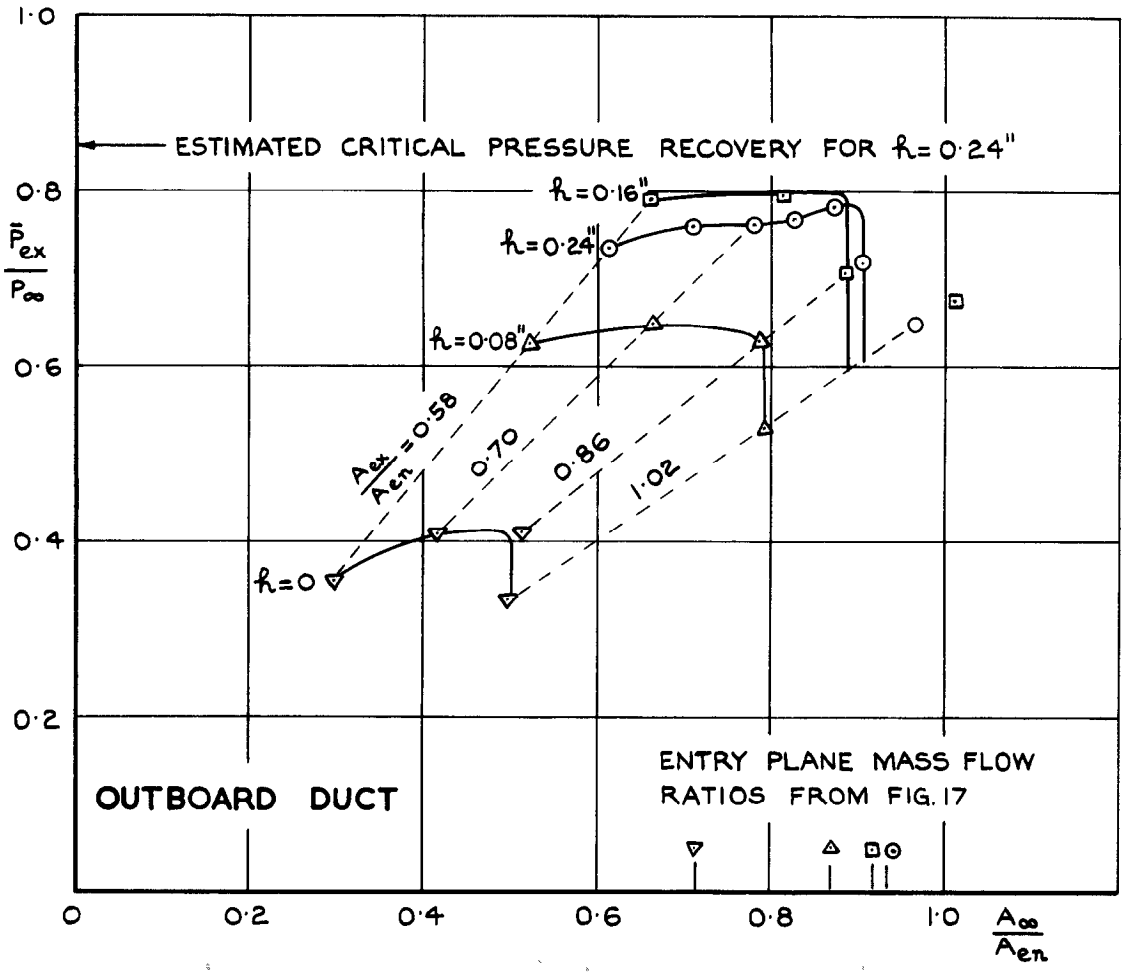

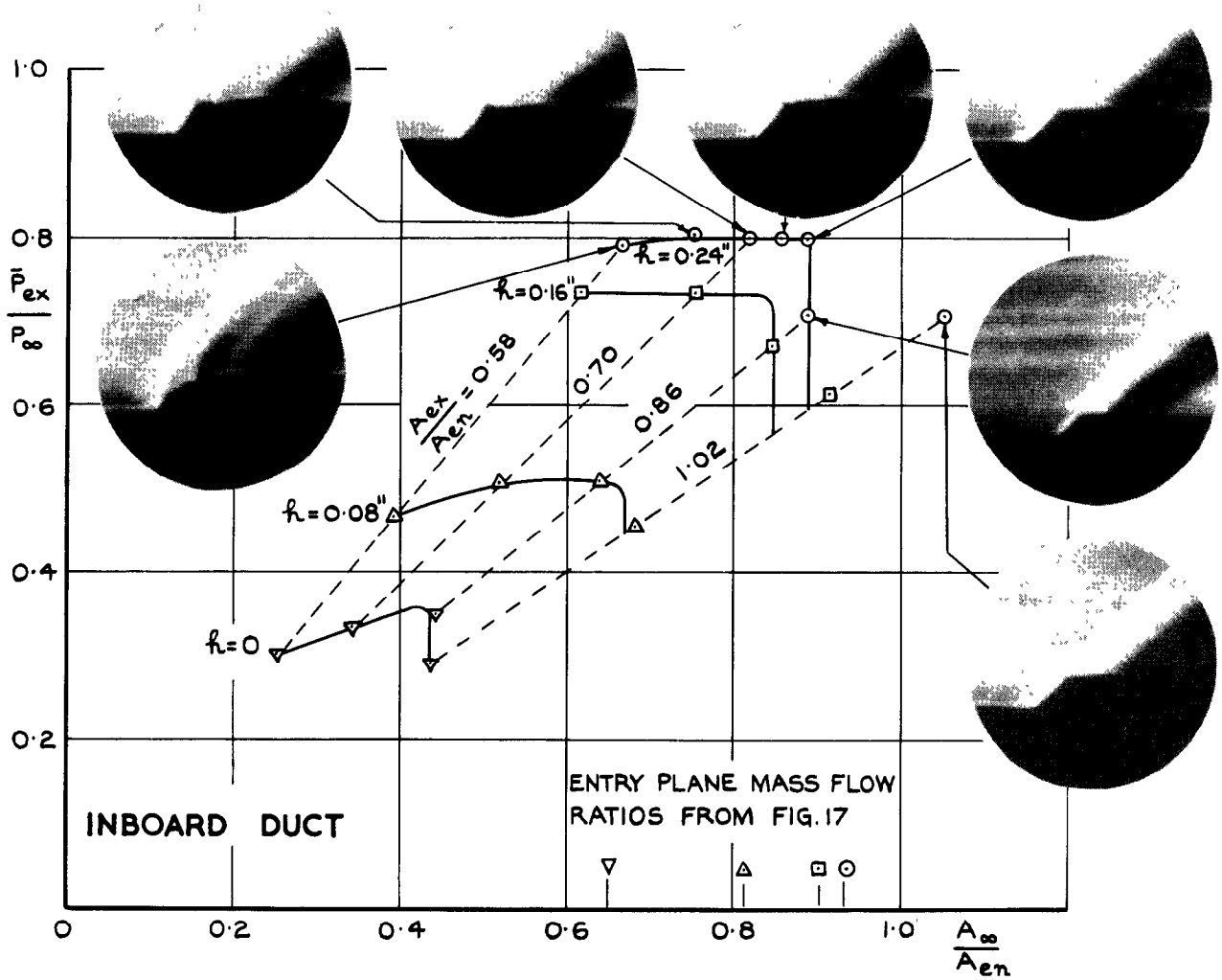

FIG.22b. VARIATION OF PRESSURE RECOVERY WITH MASS FLOW RATIO FOR α=0

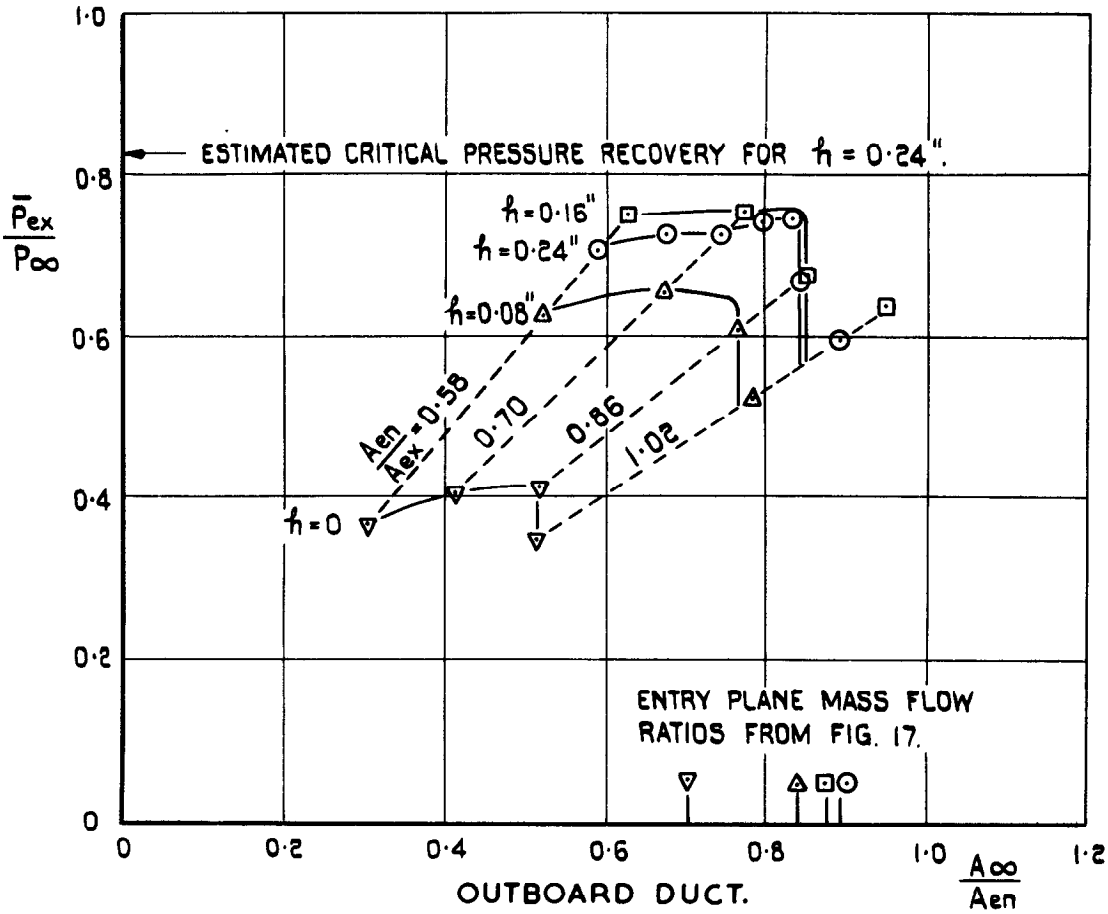

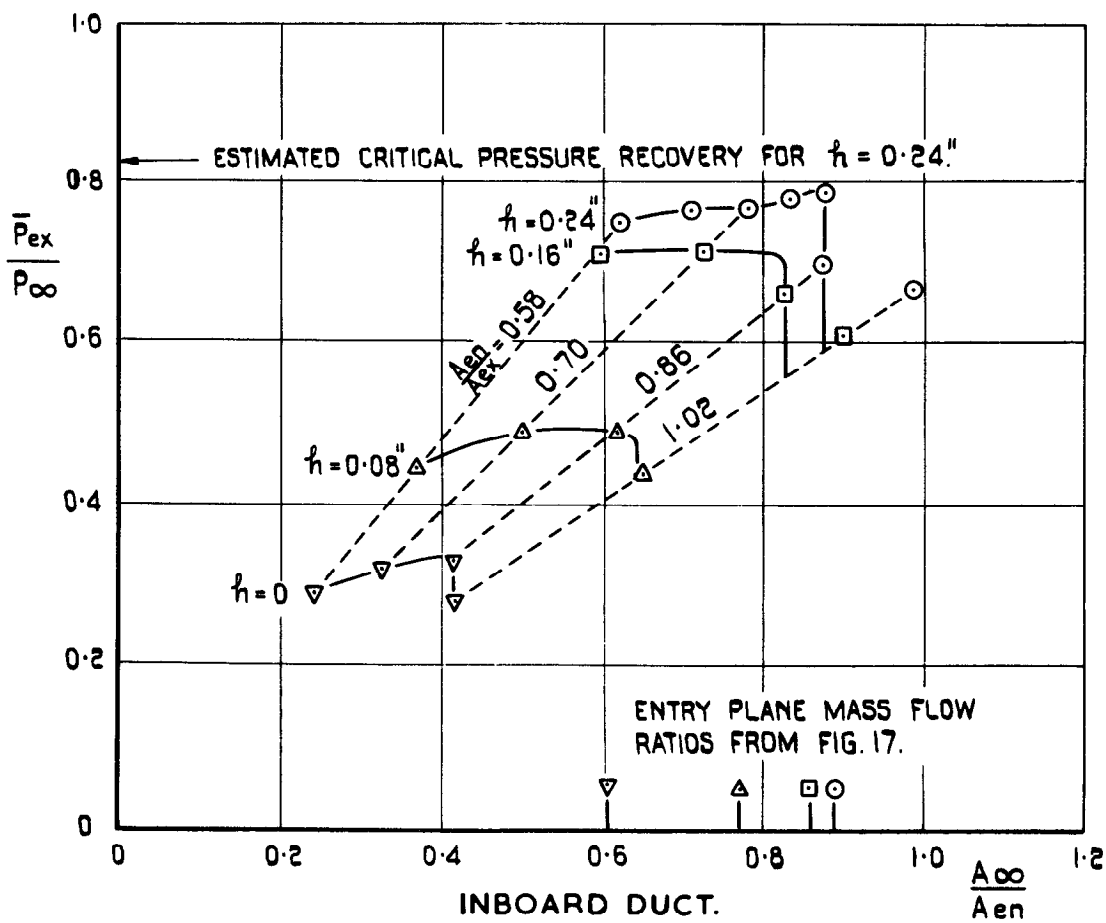

FIG. 22 (c). VARIATION OF PRESSURE RECOVERY WITH MASS FLOW RATIO FOR $\alpha = +4^\circ$.

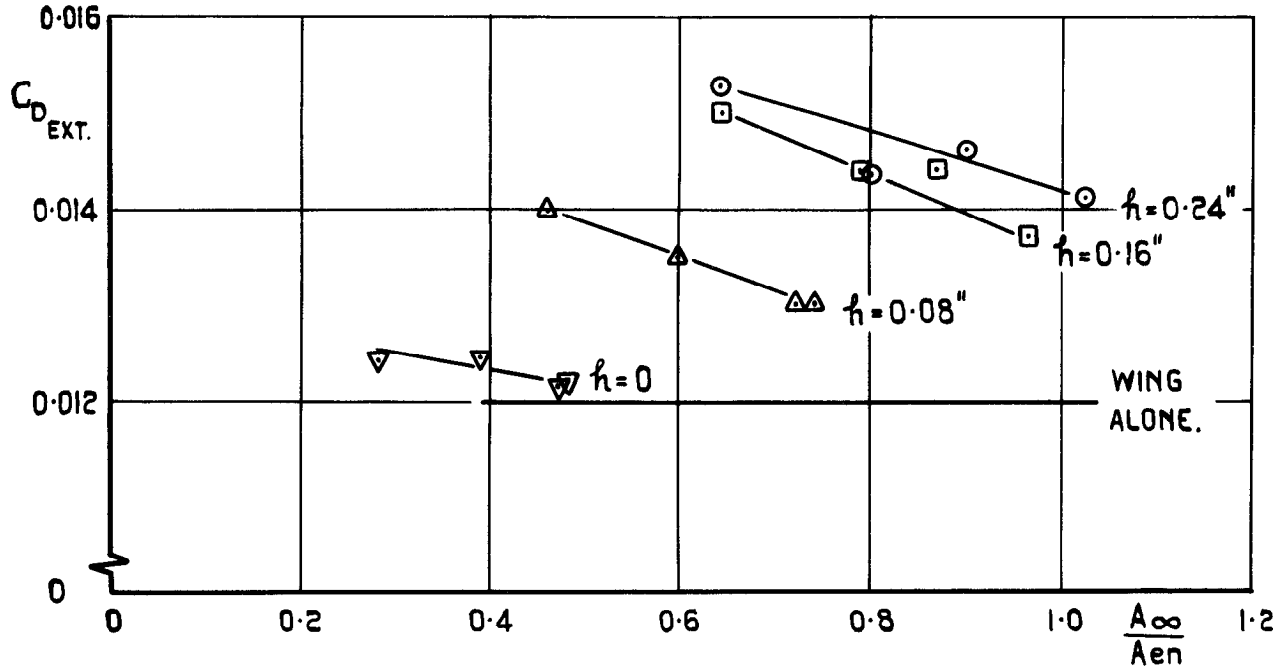

FIG. 23. VARIATION OF EXTERNAL DRAG WITH MASS FLOW AT $\alpha = 0$.

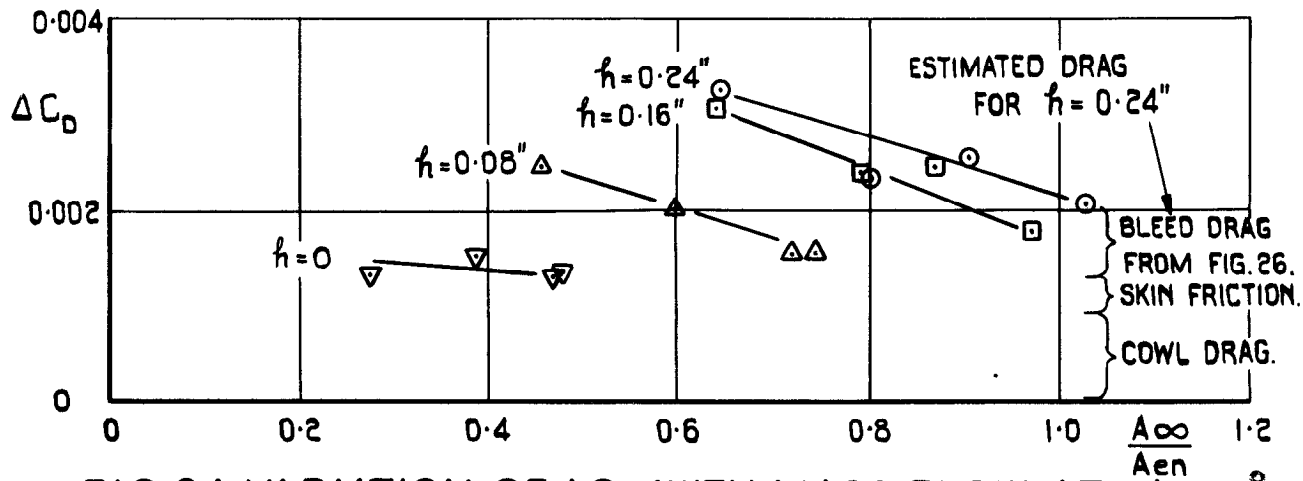

FIG. 24. VARIATION OF ΔC_D WITH MASS FLOW AT $\alpha = 0°$.

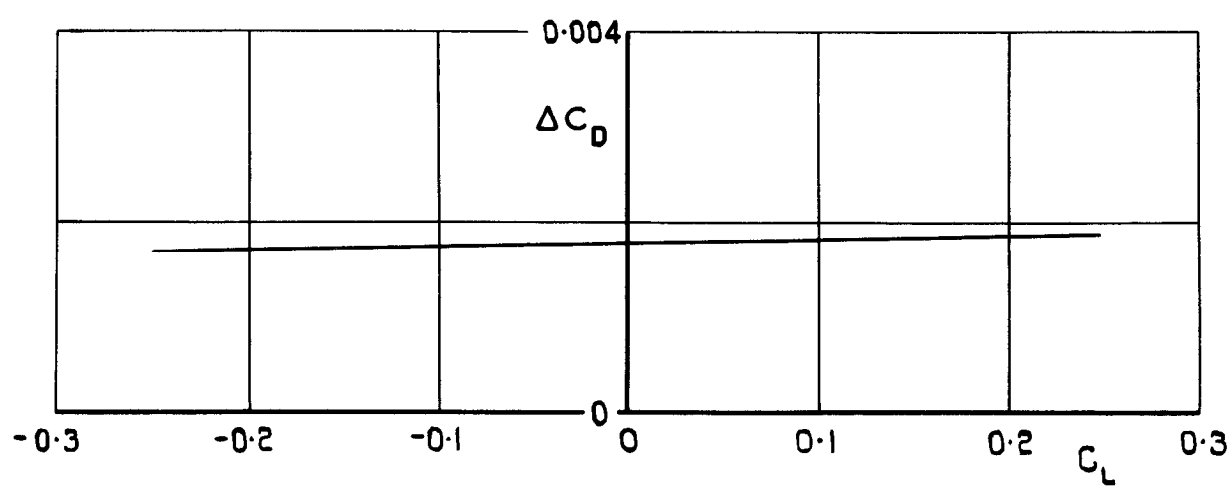

FIG. 25. VARIATION OF ΔC_D WITH C_L AT FULL MASS FLOW; h=0·16"

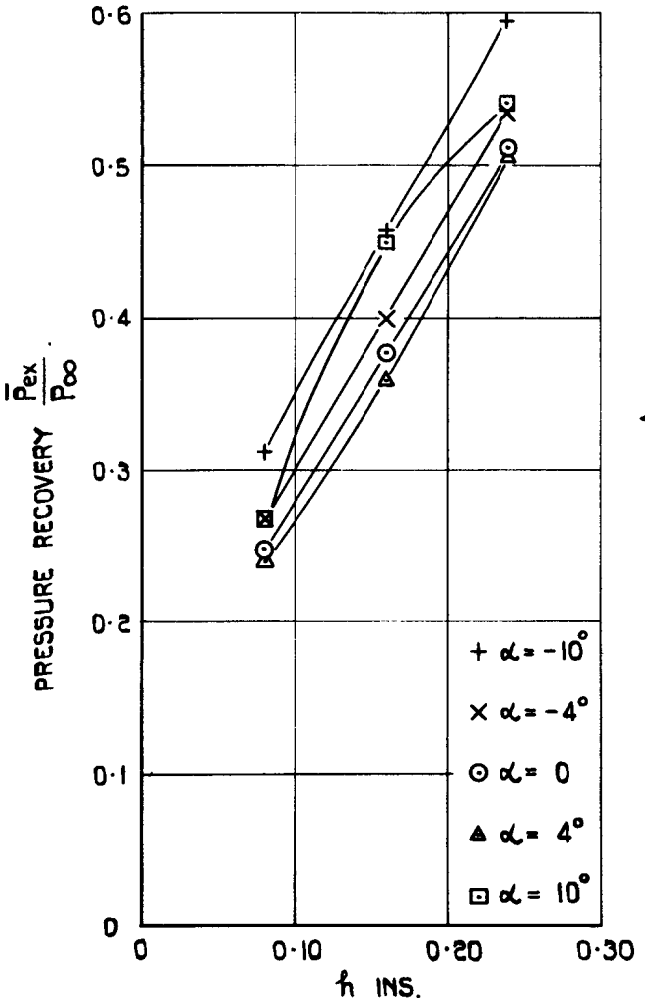

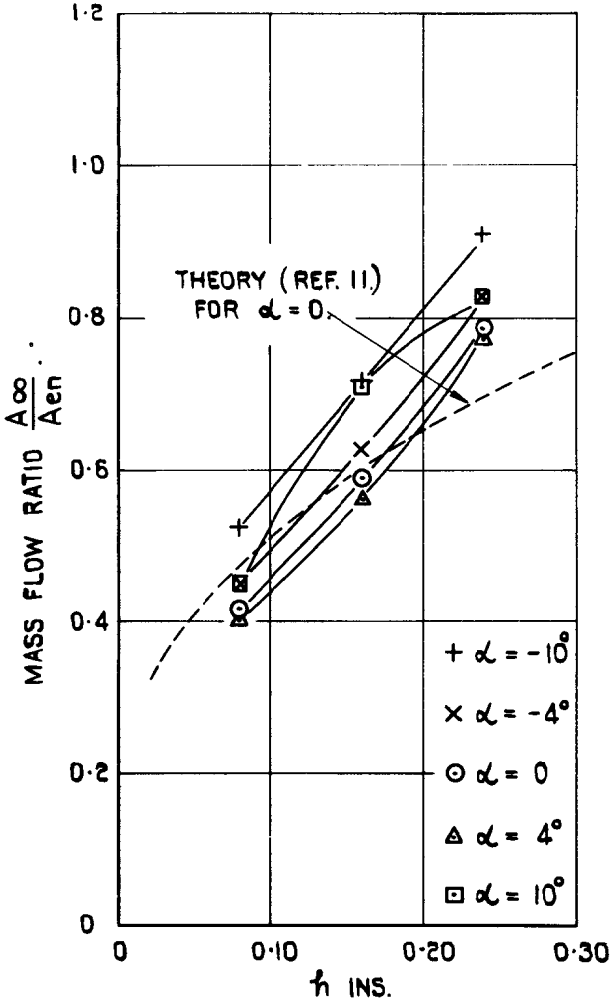

α (DEGREES)	δ (INCHES)		
	INBOARD EDGE.	OUTBOARD EDGE.	MEAN
-4	0·267	0·150	0·209
0	0·279	0·143	0·211
4	0·271	0·100	0·186
10	0·250	0·050	0·150

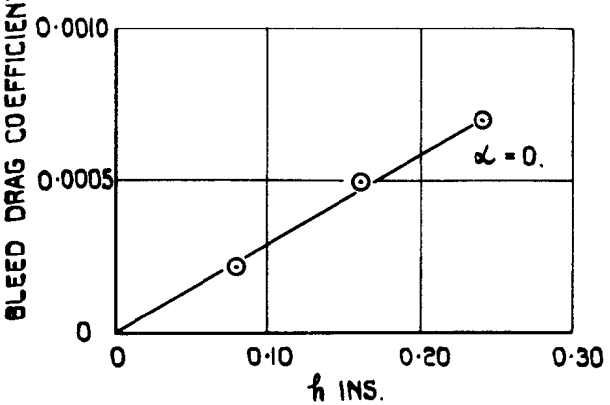

FIG. 26. BOUNDARY LAYER BLEED PERFORMANCE.

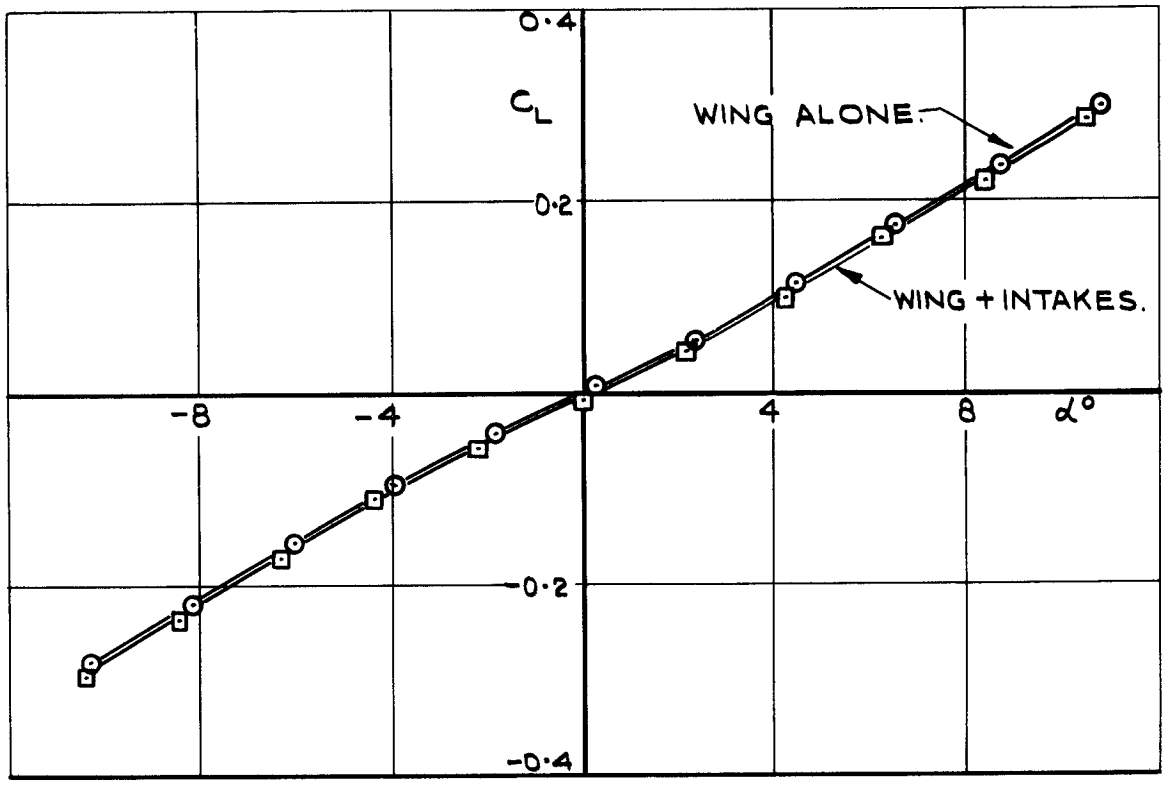

FIG. 27. VARIATION OF LIFT COEFFICIENT WITH INCIDENCE.

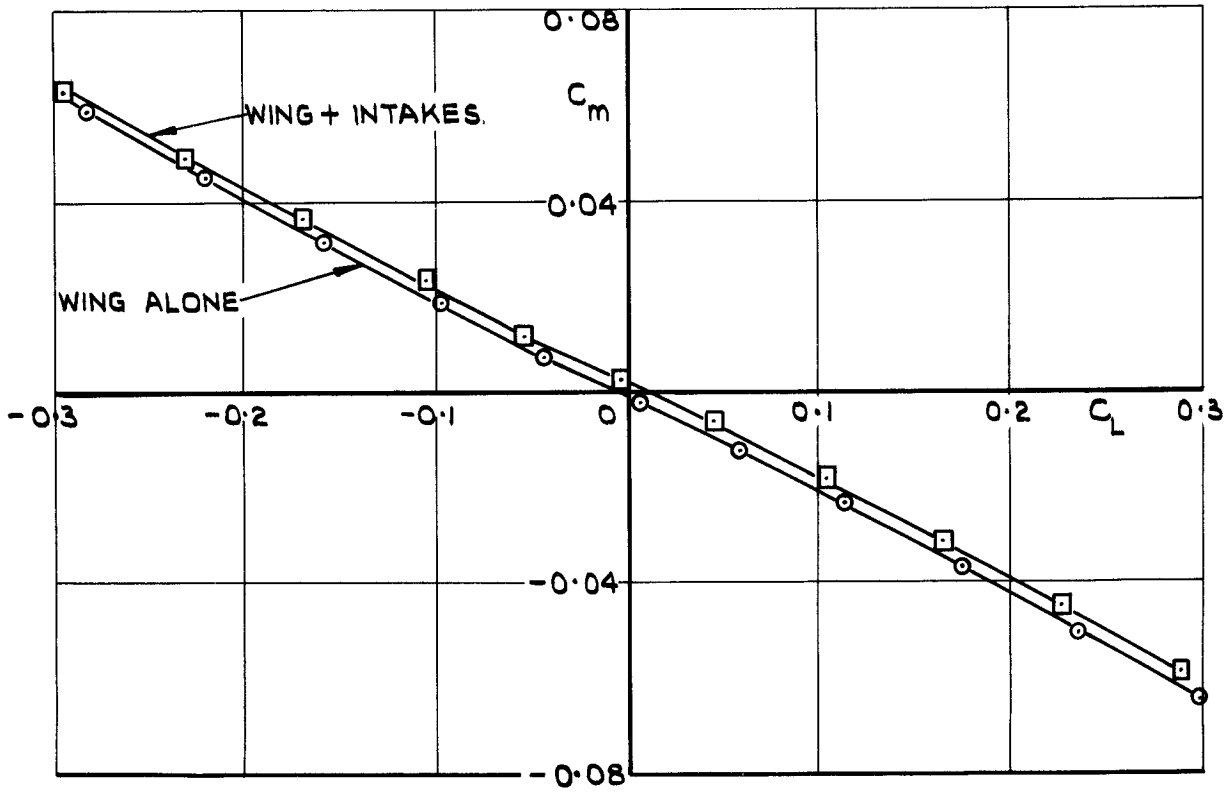

FIG. 28. VARIATION OF PITCHING MOMENT COEFFICIENT WITH LIFT COEFFICIENT.

Printed in England for Her Majesty's Stationery Office by the Royal Aircraft Establishment, Farnborough. Dd.125875. K4.

A.R.C. C.P. No. 866

533.695.17:
533.6.011.5:
533.693.3:
533.691.2

TESTS ON AN ENGINE INSTALLATION FOR A SLENDER GOTHIC WING AT M = 1.82. Griffiths, R.T. August 1964.

Tests were made at M = 1.82 over an incidence range of $\pm 10^{0}$ on an engine installation mounted at the rear of an uncambered slender gothic wing with different values of the boundary layer bleed height and at various mass flow ratios. In addition an investigation was made of the flow conditions at the inboard and outboard edges of the inlet and of the effects of the nacelles on the longitudinal characteristics of the wing. The installation represented a design in which four engines were mounted side by side in each of two nacelles, one on each half of the wing, with the engines partially buried in the wing.

It was found aerodynamically preferable to mount the engines on the lower rather than the upper surface of the wing in order to avoid the

(Over)

A.R.C. C.P. No. 866

533.695.17:
533.6.011.5:
533.693.3:
533.691.2

TESTS ON AN ENGINE INSTALLATION FOR A SLENDER GOTHIC WING AT M = 1.82. Griffiths, R.T. August 1964.

Tests were made at M = 1.82 over an incidence range of $\pm 10^{0}$ on an engine installation mounted at the rear of an uncambered slender gothic wing with different values of the boundary layer bleed height and at various mass flow ratios. In addition an investigation was made of the flow conditions at the inboard and outboard edges of the inlet and of the effects of the nacelles on the longitudinal characteristics of the wing. The installation represented a design in which four engines were mounted side by side in each of two nacelles, one on each half of the wing, with the engines partially buried in the wing.

It was found aerodynamically preferable to mount the engines on the lower rather than the upper surface of the wing in order to avoid the

(Over)

A.R.C. C.P. No. 866

533.695.17:
533.6.011.5:
533.693.3:
533.691.2

TESTS ON AN ENGINE INSTALLATION FOR A SLENDER GOTHIC WING AT M = 1.82. Griffiths, R.T. August 1964.

Tests were made at M = 1.82 over an incidence range of $\pm 10^{0}$ on an engine installation mounted at the rear of an uncambered slender gothic wing with different values of the boundary layer bleed height and at various mass flow ratios. In addition an investigation was made of the flow conditions at the inboard and outboard edges of the inlet and of the effects of the nacelles on the longitudinal characteristics of the wing. The installation represented a design in which four engines were mounted side by side in each of two nacelles, one on each half of the wing, with the engines partially buried in the wing.

It was found aerodynamically preferable to mount the engines on the lower rather than the upper surface of the wing in order to avoid the

(Over)

DETACHABLE ABSTRACT CARDS

possibility of the leading edge cortices entering the intake and to take advanrage of the reduced local Mach number present under lifting conditions. With a reasonable boundary layer bleed height, addition of the nacelles to the wing caused a 15% increase in drag, almost independent of incidence. About 30% of this increase was the drag of the boundary layer bleed duct; the remainder could be calculated closely from a knowledge of the nacelle geometry. The nacelles caused small displacements of the lift and pitching moment curves.

possibility of the leading edge vortices entering the intake and to take advantage of the reduced local Mach number present under lifting conditions. With a reasonable boundary layer bleed height, addition of the nacelles to the wing caused a 15% increase in drag, almost independent of incidence. About 30% of this increase was the drag of the boundary layer bleed duct; the remainder could be calculated closely from a knowledge of the nacelle geometry. The nacelles caused small displacements of the lift and pitching moment curves.

possibility of the leading edge vortices entering the intake and to take advantage of the reduced local Mach number present under lifting conditions. With a reasonable boundary layer bleed height, addition of the nacelles to the wing caused a 15% increase in drag, almost independent of incidence. About 30% of this increase was the drag of the boundary layer bleed duct; the remainder could be calculated closely from a knowledge of the nacelle geometry. The nacelles caused small displacements of the lift and pitching moment curves.

Published by
HER MAJESTY'S STATIONERY OFFICE
To be purchased from
49 High Holborn, London W.C.1
423 Oxford Street, London W.1
13A Castle Street, Edinburgh 2
109 St. Mary Street, Cardiff
Brazennose Street, Manchester 2
50 Fairfax Street, Bristol 1
35 Smallbrook, Ringway, Birmingham 5
80 Chichester Street, Belfast 1
or through any bookseller

C.P. No. 866

S.O. CODE No. 23-9016-66